Rep. Prog. Phys. **63** (2000) 893–938. Printed in the UK PII: S0034-4885(00)90739-5

# The physics of the near-field

Christian Girard, Christian Joachim and Sébastien Gauthier
CEMES UPR CNRS 8011, 29, rue Jeanne-Marvig, BP 4347, 31055 Toulouse Cedex 4, France

Received 8 July 1999, in final form 7 February 2000

**Abstract**

Over the last decade, extensive exploitation of the different kinds of near-fields existing spontaneously or artificially in immediate proximity to the surface of materials has generated a considerable amount of new exciting developments. In this review the main physical properties of these peculiar fields are revisited. In a first stage, following a unified pedagogical model, we recall that the concept of near-field is not restricted to specific research areas, but actually covers numerous domains of contemporary physics (electronics, photonics, interatomic forces, phononics, . . .). To a great extent, it will be shown that it mainly concerns phenomena involving evanescent fields (electronic density surface wave, evanescent light, local electrostatic and magnetic fields, . . .) or localized interatomic or molecular interactions.

In fact, the practical exploitation of these *waves* and local *interactions* was latent for a long time in physics until the beginning of the 1980s which was marked by the emergence and the success of local probe-based methods (STM, SFM, SNOM). Nowadays, various theoretical approaches and powerful numerical methods well suited to near-field physics are described in the literature. In the second part of this review, different original aspects of the near-field will be discussed with the intent of realizing control and optimization of its properties. In particular, the physics hidden inside the *inverse decay length parameter* $\eta$ associated with all near-field concepts will be analysed in detail. This analysis may serve as a general framework for the design of physical or chemical compounds (photonic and electronic) able to control this fundamental parameter.

We conclude the review by reconsidering an old and fundamental problem that can be summarized by the question, 'What happens in the near-field interaction zone?'. Actually, this problem has been largely unaddressed in the near-field literature because what is needed in most practical situations is just the transmission coefficient of the whole device. However, when some dissipative elements interact with the near-field, this reasoning appears to be somewhat limited. In order to get more insight into this challenging question, we briefly give a *state-of-the-art* review of the relation between tunnelling events and energy dissipation inside the near-field.

0034-4885/00/060893+46$90.00  

**Contents**

## 1. Introduction

The purpose of this review is to explore, deepen and unify various conceptual descriptions concerning the physics of the near-field produced or existing spontaneously at the surface or at the interface of two materials. Although near-field physics was a well established research area before the mid 1970s (Adamson 1976, Agarwal 1975, Ash and Nicholls 1972, Antoniewicz 1974, Bethe 1944, Carniglia *et al* 1972, Celli *et al* 1975, Economou and Ngai 1974, Kliewer and Fuchs 1974, Lukosz and Kunz 1977, Mavroyannis 1963, Maclachlan *et al* 1963, Mahanty and Ninham 1973, Maradudin and Zierau 1976, Otto 1968, Ruppin 1973, Steele 1974), its actual and systematic investigation began only 18 years ago with the invention of the scanning tunnelling microscope (STM) (Binnig and Rohrer 1982, Binnig *et al* 1982, Behm *et al* 1990). Within a few years of this important discovery, the broadcasting of its impressive achievements and measurements around the world had given rise to an explosion of new experimental devices (Binnig *et al* 1986, Pohl *et al* 1984, Dürig *et al* 1986, Güntherodt *et al* 1995) able to explore and measure many different kinds of near-fields (electronic, photonic, acoustic, force, ...).

### *1.1. Basic concepts and definitions*

It has long been known that the surface limiting a solid body locally modifies the physical properties of many materials (dielectric, metal, or semiconductor) (Zangwill 1988). In other words, the symmetry loss generated by the presence of an interface produces specific surface phenomena that have been well identified in the past (spontaneous polarization, electronic work function, electronic surface states, surface polaritons, surface enhanced optical properties, ...).

The near-field can be defined as the extension outside a given material of the field existing inside this material. Basically, it results from the linear, homogeneous and isotropic properties of the *space–time* that impose a continuous variation of field amplitudes and energies across the interfaces. In most cases, the amplitude of the near-field decays very rapidly along the direction perpendicular to the interface giving rise to the so-called evanescent wave character of the near-field.

In optics, the symmetry reduction occurring in the vicinity of an interface can enhance some hyperpolarizabilities initially absent in the bulk materials. This has been used for surface second-harmonic generation at the metal–air interface (Furtak and Reyes 1980). In the vicinity of a metal–vacuum interface, the electron density distribution tails off exponentially into the vacuum and exhibits Friedel oscillations on the metal side (Ziman 1964, Lang 1969). A long list of similar effects extensively described in the *surface science literature* arise due to the existence of this near-field zone. In this context, surfaces can also be considered as a privileged place to generate, guide, manipulate and detect evanescent waves.

### *1.2. Objectives*

The main objective of this review is to discuss the similarities and the fundamental differences between different kinds of near-fields. The discussion is constructed around a limited number of typical examples borrowed from surface physics. In this domain, the research literature has developed explosively and given rise to a huge amount of peculiar results. Whenever possible, we emphasize the common features that govern their physical properties (shape, localization, polarization, decay length, ...). Furthermore, since this review is multidisciplinary, a special effort has been made to expose a large part of the theoretical background with simple and analytical formalisms.

Four different kinds of near-fields are treated in section 2: namely, the electrostatic surface field, the optical near-field, the fluctuating electromagnetic field and finally the electronic evanescent wavefunction near metallic surfaces. Although many other particular cases might be analysed, this limited selection provides a good insight into this research field. This introductory classification is then used in section 3 to discuss and illuminate some intrinsic properties of these near-fields.

The main mechanisms responsible for the detection of the near-field are detailed in section 4 and other original aspects of the near-field are discussed in section 5. In particular, the physics hidden inside the *inverse decay length parameter* $\eta$ associated with all near-field concepts, will be analysed in a detailed manner. This analysis will serve as a general framework to design physical or chemical compounds (electronic and photonic) able to optimize this fundamental parameter. These two parts (sections 4 and 5) introduce logical and readable presentations of the basic concepts inherited from two currently available *real-space approaches*, namely the localized Green function (LGF) (Lucas *et al* 1988, Girard 1992) and elastic scattering quantum chemistry (ESQC) (Sautet and Joachim 1991). These frameworks serve to stress the equivalence between scattering and localized states theories. Finally, a brief insight into recent and new attempts at energy dissipation calculations in an evanescent regime is provided in section 6.

The material covered in the review should be of direct interest to a broad range of people working with different local probe-based methods (LPBMs) but could also be attractive to the physicist communities concerned with resonant and nonresonant tunnel transfer (electronic, photonic or excitonic).

## 2. The different categories of near-fields

According to our previous definition (see section 1.1), a given field $\mathcal{F}(\boldsymbol{r})$ lying in a spatial region $(A)$ always presents a continuous extension inside an adjoining domain $(B)$. This proposition is true whatever the change between the physical properties of the two regions $(A)$ and $(B)$ may be. In well defined conditions, this leads to the occurence of a more or less rapid decay of the field $\mathcal{F}(\boldsymbol{r})$ inside the domain $(B)$. We can distinguish two important categories of such interfacial near-fields.

(i) The first corresponds to spontaneous near-fields produced in $(B)$ from a permanently established field in $(A)$. For example, permanent electric fields in immediate proximity to an ionic crystal belong to this category. This is also the case of the wavefunctions of electrons that tail off the surface of a metal. More subtle are the spontaneous surface electromagnetic fields because they result from the correlation of fluctuating densities of charges inside the materials. Although not directly accessible, they are responsible for near-field dispersion effects, such as the van der Waals force field and the spontaneous interfacial polarization of the free surface of a dielectric.

(ii) The second class gathers together surface near-fields that can only be produced by applying an external excitation (photon and electron beams impinging on a surface). Both optical near-fields and surface plasmon-polaritons excited at a solid interface provide good illustrations of this category. These phenomena have a special interest because they can be manipulated at will by an external operator.

In sections 2.1–2.4 four typical examples belonging to these two families are surveyed. We have made a special effort to present these phenomena from an unified point of view based on simple theoretical concepts.

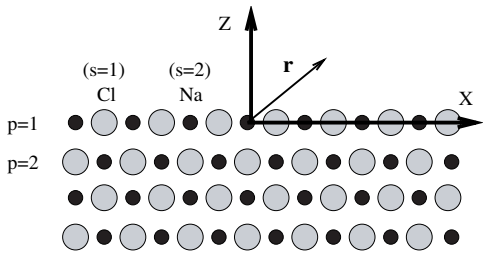


**Figure 1.** Schematic drawing of an NaCl crystal. The large circles represent the $Cl^-$ ions, the small circles represent the the $Na^+$ ions.

### *2.1. Electrostatic surface fields*

A simple example of permanent electric near-field can be found close to the surface of ionic or metal oxide crystals (NaCl, LiF, MgO, ...). We focus mainly on the case of the (100) NaCl surface.

Following the pioneering works of Born and Madelung, it is well known that the NaCl crystal stability results from a subtle competition between long-range Coulomb and short-range core–core interactions. It was soon recognized that the surface atoms produce an electric field $\boldsymbol{E}(\boldsymbol{r})$ localized at the vacuum–NaCl(100) interface whose the associated electric potential $\mathcal{V}(\boldsymbol{r})$ can be merely described by adding the individual charge contributions of each atom. The electric potential at a point $\boldsymbol{r} = (x, y, z > 0) = (\boldsymbol{l}, z)$ lying above the surface is given by

$$\mathcal{V}(\boldsymbol{r}) = \sum_{\alpha,\beta} \sum_{s,p} L_p \frac{q_s}{|\boldsymbol{r} - \boldsymbol{r}_{s,p,\alpha,\beta}|}. \tag{1}$$

The $(s, p)$ atom is the $s$th atom of the two-dimensional (2D) primitive cell pertaining to the $p$th plane parallel to the surface and located at a distance $z_p$ from it. The indices $(\alpha, \beta)$ serve to label primitive surface cells pertaining to a given plane $(p)$. We can write

$$\boldsymbol{r}_{s,p,\alpha,\beta} = \alpha(A, 0) + \beta(0, A) + \boldsymbol{u}_{s,p} - (p-1)D\boldsymbol{u}_z \tag{2}$$

where $A$ is the surface lattice parameter (3.99 Å for NaCl), $\boldsymbol{u}_z$ is a unit vector perpendicular to the surface, and $D$ represents the spacing between two consecutive planes. The factor $L_p$ accounts for the screening effect on the charges due to the surroundings as viewed by a test point outside the solid (Girard and Girardet 1987), and the charge $q_s$ is related to the $s$th atom of the surface primitive cell (see figure 1). For the (100) face of an ionic crystal, the translation vector is related to the lattice parameter $A$ by

$$\boldsymbol{u}_{s,p} = \left(\frac{A}{2}, \frac{A}{2}\right)[1 - (-1)^{s+p}]. \tag{3}$$

In order to benefit from the surface periodicity, equation (1) may be rewritten as a summation in the surface reciprocal space $\{\boldsymbol{g}\}$,

$$\mathcal{V}(\boldsymbol{r}) = \frac{2\pi}{A^2} \sum_{s,p} \sum_{\boldsymbol{g}} L_p q_s \exp(-g(z - z_p)) \frac{\exp[\mathrm{i}\boldsymbol{g} \cdot (\boldsymbol{l} + \boldsymbol{u}_{s,p})]}{g} \tag{4}$$

where the reciprocal lattice vectors $\boldsymbol{g}$ are generated by two integer numbers $g_1$ and $g_2$:

$$\boldsymbol{g} = \frac{2\pi}{A}(g_1, g_2). \tag{5}$$

The two major contributions of (4) yielded by the two first-surface harmonics (1, 0) and (0, 1) lead to a simple expression

$$\mathcal{V}(\boldsymbol{r}) = \frac{1}{A} \sum_{p=1}^{\infty} L_p \exp\left[-\frac{2\pi}{A}(z + (p-1)D)\right] \mathcal{F}_p(x, y) \tag{6}$$

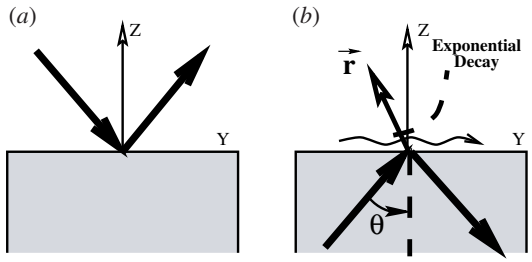


**Figure 2.** Schematic drawing of two illumination configurations. (*a*) External reflection; (*b*) total internal reflection.

where the corrugation potential profile is given by

$$\mathcal{F}_p(x, y) = \sum_{s=1,2} q_s \left\{ \cos\left(\frac{2\pi}{A}(x + u^x_{s,p})\right) + \cos\left(\frac{2\pi}{A}(y + u^y_{s,p})\right)\right\}. \tag{7}$$

Outside the crystal, the components of the electric field $\boldsymbol{E}(\boldsymbol{r}) = -\nabla\mathcal{V}(\boldsymbol{r})$ derived from the local ionic potential (6) decay exponentially ($\exp(-2\pi z/A)$). This is a static and permanent near-field with an inverse decay length $\eta = 2\pi/A$. For the (100) face of NaCl this parameter is equal to 1.574 $\text{Å}^{-1}$ and at 3 Å from the outmost surface atoms the $E_z(\boldsymbol{r})$ component can reach 2.5 V $\text{Å}^{-1}$.

Several others permanent surface electric fields have been identified (Adamson 1976). For example, the well known electric superficial polarization generated by fatty acid molecules films adsorbed on the surface of water belongs to this familly of *electric near-field*. Similarly, the permanent dispersion polarization that originates from the zero-point quantum fluctuation surface electromagnetic modes also generates a *surface electric near-field* displaying similar features (Galatry and Gharbi 1981).

### *2.2. Optical near-fields*

Optical nonfluctuating near-fields are not permanent and consequently must be generated by an external light source. The simplest method consists of illuminating the surface of a sample by external reflection. In this case, the structure of the electromagnetic field ($\boldsymbol{E}_0$, $\boldsymbol{B}_0$) above the sample critically depends on the incident angle. This effect is particularly important outside the Brewster angle, where the field intensity tends to be modulated by the interferences between incident and reflected waves (see figure 2(*a*)). Another way to illuminate a transparent sample is by total internal reflection (TIR). In this configuration, the illuminating field is incident below the surface at an angle larger than the TIR angle $\theta_{\text{tot}}$. In this way, the excitation field above the surface becomes an evanescent surface wave (see figure 2(*b*)). The physics of optical evanescent waves (OEWs) which is the central concept used in near-field optics (NFO) instrumentation has been familiar in traditional optics for a long time (Courjon and Bainier 1994). The analysis of the skin depth effect at metallic surfaces was probably the first recognition of the existence of evanescent electromagnetic waves (Zenneck 1907, Sommerfeld 1909).

In the basic TIR configuration (see figure 2(*b*)), the surface wave is generated by illuminating the surface from underneath by a monochromatic planewave of frequency $\omega_0$, incident at an angle $\theta$ larger than $\theta_{\text{tot}}$. Two different incident polarizations can be considered: s polarization, where the incident electric field is parallel to the surface–air interface and p polarization, where it is in the plane of incidence.

The incident field at an observation point $\boldsymbol{r} = (x, y, z) = (\boldsymbol{l}, z)$ above the surface becomes

$$\boldsymbol{E}_{\mathrm{o}}(\boldsymbol{r}, t) = \boldsymbol{E}_{\mathrm{o}}(\boldsymbol{r})\mathrm{e}^{-\mathrm{i}\omega_0 t} = \boldsymbol{E}_{\mathrm{o}}\mathrm{e}^{\mathrm{i}\boldsymbol{k}\cdot\boldsymbol{l}}\mathrm{e}^{-\eta z}\mathrm{e}^{-\mathrm{i}\omega_0 t}, \tag{8}$$

where

$$\eta = \frac{\omega_0}{c}(\sin^2\theta - \sin^2\theta_{\mathrm{tot}})^{1/2} \tag{9}$$

and

$$\|\boldsymbol{k}\| = \frac{\omega_0}{c}\sin\theta. \tag{10}$$

When, for example, the incident field is propagating along the OY axis, one obtains for s polarization:

$$\begin{aligned} E_{0x}(\boldsymbol{r}) &= A_0 T_s \\ E_{0y}(\boldsymbol{r}) &= E_{0z}(\boldsymbol{r}) = 0; \end{aligned} \tag{11}$$

and for p polarization:

$$\begin{aligned} E_{0x}(\boldsymbol{r}) &= 0 \\ E_{0y}(\boldsymbol{r}) &= A_0 T_p \delta_c \\ E_{0z}(\boldsymbol{r}) &= A_0 T_p \delta_s; \end{aligned} \tag{12}$$

where

$$\begin{aligned} \delta_s &= \frac{\sin(\theta)}{\sin(\theta_{\mathrm{tot}})}, \\ \delta_c &= \frac{\mathrm{i}\eta}{k_0 \sin(\theta_{\mathrm{tot}})}. \end{aligned} \tag{13}$$

In equations (11) and (12), $A_0$ is proportional to $\mathrm{e}^{\mathrm{i}ky}\mathrm{e}^{-\eta z}$, and the factors $T_s$ and $T_p$ are the usual transmission coefficients for each polarization (Born and Wolf 1964). From Maxwell's equations and relations (8), (11) and (12), we can easily deduce the magnetic field $\boldsymbol{B}_0(\boldsymbol{r})$ associated with the surface wave:

$$\boldsymbol{B}_0(\boldsymbol{r}, t) = \frac{c}{\mathrm{i}\omega_0}\nabla \wedge \boldsymbol{E}_0(\boldsymbol{r}, t). \tag{14}$$

These last four equations completely define the electromagnetic state of the surface evanescent wave. As previously, the inverse decay length $\eta$ of the electromagnetic evanescent field can be defined by analysing either the variations of the electric or magnetic field intensities when getting closer and closer to the sample. For the perfectly planar surface considered in this section, $\eta$ does not depend on the polarization state. It just depends on the optical index variation (implicitly contained in the parameter $\theta_{\mathrm{tot}}$) and, as described in figure 3, on the incident angle $\theta$. Near the grazing angle ($\theta \sim 90^\circ$) this parameter takes large values and the optical evanescent wave vanishes.

In modern physics, the control of such peculiar light fields provides an interesting and versatile tool that generates powerful applications (tunnelling time measurements (Balcou and Dutriaux 1997), highly resolved microscopy and spectroscopy (Pohl and Courjon 1993), and surface plasmon resonance spectroscopy of molecular adlayers (Jung *et al* 1998), atomic physics (Landragin *et al* 1996, Esslinger *et al* 1993)). For example, in *laser-cooled atoms* physics such phenomena can be used as adjustable 'atomic mirrors'. Under certain conditions, it is even possible, by adjusting the force field associated with the OEW to balance the van der Waals forces between a small number of cooled atoms and the neighbouring surface. The control of the different optical parameters (incident angle, polarization, wavelength, ...) leads to new noninvasive atomic manipulation processes (Landragin *et al* 1996).

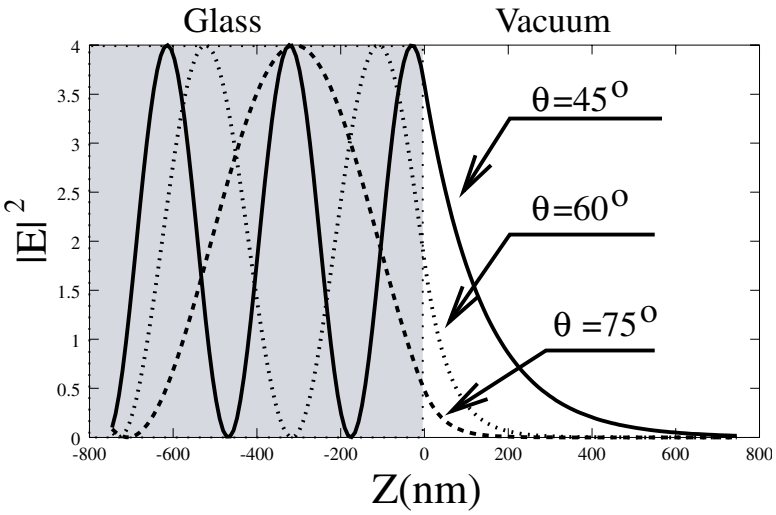


**Figure 3.** Illustration of the exponential decay variation versus the incident angle. The glass sample of optical index $n = 1.5$ ($\theta_{\text{tot}} = 41.8°$) is illuminated in TIR (s-polarized mode).

### *2.3. Electromagnetic fluctuating near-field*

We consider now a less conventional class of surface near-fields, that nonetheless have a considerable impact in local probe-based experiments. It concerns the fluctuating electromagnetic field existing spontaneously near the surface of any material. Historically, as early as 1930, London showed that the quantum mechanical fluctuations between two neutral atoms or molecules (devoid of any permanent multipole moments and separated by a distance $R$) could give rise to a force which varies as $R^{-7}$ (London 1930). Two decades later this concept was generalized by Lifshitz in order to derive a complete scheme able to grasp the origin of van der Waals dispersion forces between solid bodies (Lifshitz 1956). This author explained these forces by a complicated Green function investigation of coherent fluctuations in the solutions of Maxwell equations. Nowadays, the theory of van der Waals forces as well as related dispersion effects are well established and extensively described in the literature (Mahanty and Ninham 1976). In addition, several direct and indirect measurements of these effects have been reported (Sabisky and Anderson 1973, Israelachvilli and Adams 1976, Tabor and Winterton 1969, Lamoreaux 1997).

Actually, the existence of fluctuating near-fields (FNFs) $\{\boldsymbol{E}_1(t);\ \boldsymbol{E}_2(t)\}$ localized in immediate proximity to the surface of a solid body is responsible for several original near-field effects (see figure 4). For instance, the atom–surface dispersion force (Maclachlan *et al* 1963), the long-range polarization induced by adsorption (Antoniewicz 1974), and the dispersion surface energy effect (Mahanty and Ninham 1973) belong to this family. In each case, the relevant effect is governed by a same correlation function $\mathcal{E}$ built from the mean square of the fluctuating electric field $\boldsymbol{E}_2(\boldsymbol{r}, \boldsymbol{r}', \omega)$ occurring in the vacuum side. It may be defined by

$$\mathcal{E}(\boldsymbol{r}', \boldsymbol{r}'', \omega', \omega'') = \text{Tr}\langle \boldsymbol{E}_2(\boldsymbol{r}', \omega')\boldsymbol{E}_2(\boldsymbol{r}'', \omega'')\rangle. \tag{15}$$

In this definition, $\boldsymbol{E}_2(\boldsymbol{r}', \omega')$ represents the Fourier transform of the electric field operator $\boldsymbol{E}_2(\boldsymbol{r}', t)$ associated with the solid. The brackets in (15) mean both statistical and quantum average on the corresponding states (Landau and Lifshitz 1960b). Therefore, according to the fluctuation–dissipation theorem (Landau and Lifshitz 1960b), this quantity can be related to

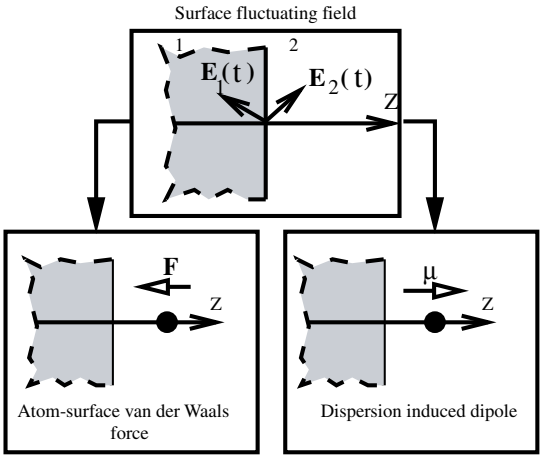


**Figure 4.** Schematic illustration of the role played by the fluctuating electric surface near-field on both electrical and mechanical properties of a physisorbed atom.

the imaginary part of the field susceptibility $\boldsymbol{S}(\boldsymbol{r}', \boldsymbol{r}'', \omega)$ of the surface. In order to achieve this transformation, we first express explicitly the average given in (15)

$$\langle \boldsymbol{E}_2(\boldsymbol{r}', \omega')\boldsymbol{E}_2(\boldsymbol{r}'', \omega'')\rangle = \tfrac{1}{2}\sum_r \rho_r^{(s)} \langle r|[\boldsymbol{E}_2(\boldsymbol{r}', \omega'), \boldsymbol{E}_2(\boldsymbol{r}'', \omega'')]_+|r\rangle \tag{16}$$

where $\rho_r^{(s)}$ represents a diagonal term of the the density matrix associated with the surface. Following some usual procedures described in the literature (see, for example, Landau and Lifshitz (1960b)), this quantity can be merely expressed in terms of both the eigenenergies $U_r^{(s)}$ of the isolated system and of its free energy $F_s$:

$$\rho_r^{(s)} = \exp[(F_s - U_r^{(s)})/K_B T]. \tag{17}$$

Finally, after some algebraic manipulation we can write

$$\mathcal{E}(\boldsymbol{r}', \boldsymbol{r}'', \omega', \omega'') = \frac{\hbar}{2\pi} \coth\left\{\frac{\hbar\omega}{2K_B T}\right\} \mathrm{Im}\,[\mathrm{Tr}\,\boldsymbol{S}(\boldsymbol{r}', \boldsymbol{r}'', \omega')]\delta(\omega' + \omega''). \tag{18}$$

The field susceptibility $\boldsymbol{S}$ that enters this equation reveals how a dipolar source field that fluctuates at the frequency $\omega'$ is modified by the proximity of the surface limiting the system. In a general quantum description, this response function can be expressed in terms of the matrix elements $\boldsymbol{E}_2^{or}$ of the field operator $\boldsymbol{E}_2$ associated with the material system (Agarwal 1975, Agarwal 1977, Metiu 1984, Girard 1986):

$$\boldsymbol{S}(\boldsymbol{r}', \boldsymbol{r}'', \omega) = \frac{1}{\hbar}\sum_r \rho_r^{(s)} \left\{\frac{\boldsymbol{E}_2^{or}(\boldsymbol{r}', \omega')\boldsymbol{E}_2^{ro}(\boldsymbol{r}'', \omega'')}{\omega - \omega_{ro}} - \frac{\boldsymbol{E}_2^{or}(\boldsymbol{r}'', \omega'')\boldsymbol{E}_2^{ro}(\boldsymbol{r}', \omega')}{\omega + \omega_{ro}}\right\}. \tag{19}$$

The deduction of the response field of the solid to a fluctuating dipole moment is another way of deriving this susceptibility. In the particular case of a solid limited by a perfectly planar surface, various theoretical methods have been developed to derive this dyadic tensor (Metiu 1984). In the framework of the local approximation, it is merely related to the frequency-dependent dielectric constant $\epsilon(\omega)$ of the material:

$$\boldsymbol{S}(\boldsymbol{r}', \boldsymbol{r}'', \omega) = \frac{\epsilon(\omega) - 1}{\epsilon(\omega) + 1} \frac{1}{(X^2 + Y^2 + Z^2)^{5/2}} \times \begin{pmatrix} Z^2 + Y^2 - 2X^2 & 3XY & 3XZ \\ -3XY & Z^2 + X^2 - 2Y^2 & 3YZ \\ -3XZ & -3YZ & 2Z^2 - Y^2 - X^2 \end{pmatrix} \tag{20}$$

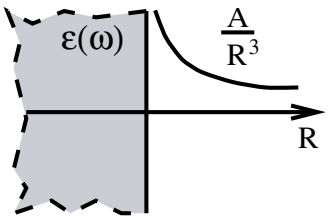


**Figure 5.** Illustration of the $R^{-3}$ dependence of the mean square fluctuating field $\mathcal{E}$ induced by the presence of a plane dielectric surface.

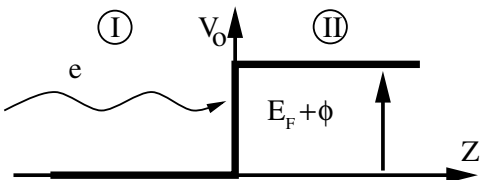


**Figure 6.** Schematic drawing of the surface barrier as seen by free electrons. The origin of the energy is chosen at the bottom of the conduction band.

where, for the sake of simplicity, we have introduced three reduced variables defined from $\boldsymbol{r}' = (x', y', z')$ and $\boldsymbol{r}'' = (x'', y'', z'')$, namely $X = x' - x''$, $Y = y' - y''$, and $Z = z' + z''$. Note that the second-rank tensor (equation (20)) contains, through the frequency-dependent dielectric constant $\epsilon(\omega)$, all information about the dynamic response of the solid. Now, we have all the ingredients we need to get more insight into the correlation function behaviour (equation (15)). To make the discussion easy we restrict ourselves to the particular case where the two locations $\boldsymbol{r}'$ and $\boldsymbol{r}''$ coincide, i.e. when $\boldsymbol{r}' = \boldsymbol{r}'' = (0, 0, R)$. In this case, the correlation function defined from relations (15), (18) and (20) reduces to

$$\mathcal{E}(R, \omega', \omega'') = \frac{\hbar}{4\pi R^3} \coth\left\{\frac{\hbar\omega}{2K_B T}\right\} \delta(\omega' + \omega'') \mathrm{Im}\left[\frac{\epsilon(\omega') - 1}{\epsilon(\omega') + 1}\right]. \tag{21}$$

As expected, this kind of correlation function generates the typical spatial decay ($\simeq R^{-3}$, see figure 5) of the van der Waals dispersion energy ($U_{vdw} = -C_3/R^{-3}$) between a single atom and a planar surface (Mavroyannis 1963). Note that this equivalence is strictly verified only if the multiple reflections occurring between the atom and the surface are neglected in the calculation of dispersion energy $U_{vdw}$. To conclude this part, let us underline that this FNF it is not directly observable. Nevertheless, it can be converted into measurable physical quantities (atomic force, atomic induced dipole moment, ...). In these two examples, the spatial decay will be governed by the first gradient of the correlation function $\mathcal{E}$.

### *2.4. Electronic wavefunction at a metal surface*

Before beginning with this last example it is appropriate to briefly outline what is known theoretically about the surface charge density near metal. The metal–vacuum interface can be merely described with the free-electron Sommerfeld approximation (FESA) in which the ground state properties of the electron gas are obtained by filling up the conduction band with $N$ free electrons obeying a Fermi–Dirac distribution (Ashcroft and Mermin 1968). This free-electron scheme can be completed by applying the density functional method inside a 'jellium' environment in which the ion cores are smeared out into a uniform positive background truncated by the surface. The electron charge profile near various metal surfaces was calculated with this technique by Lang and Kohn. It shows up the splitting between delocalized electronic charges and positive 'jellium' into the vacuum side of the interface. In the metal, it exhibits the well known Friedel oscillations, which have the characteristic wavelength $\pi/K_F$ ($K_F$ is the Fermi wavevector). Typical curves displaying these features have been gathered in Lang (1994) with additional information on the application of this model to the theory of single-atom STM imaging. This method has been improved in order to account for the discrete nature of both substrates and adsorbates (Tsukada *et al* 1991b).

To illustrate and get more insight into this kind of *surface near-field* we continue our discussion with the pedagogical FESA model. Let us consider the idealized metal–vacuum interface depicted in figure 6. The metal surface experienced by the free electrons is represented by a finite step potential in which the *energy origin*

$$\begin{aligned} V_0(z) &= 0, \qquad (z < 0), \\ V_0(z) &= \phi + E_F, \qquad (z > 0), \end{aligned} \tag{22}$$

where $\phi$ is the work function and $E_F = \hbar K_F^2/2m$ is the Fermi level of the metal. We first solve the Schrödinger equation for each of the two regions (I) and (II). Furthermore, we look for solutions for incident electrons with energies $E = E_\perp + E_\parallel$ adapted to the planar geometry under consideration:

$$\Psi(\boldsymbol{l}, z) = \frac{1}{v^{1/2}} \psi_{I/II}(z) \exp(\mathrm{i}\boldsymbol{k}_\parallel \cdot \boldsymbol{l}), \tag{23}$$

where $v$ represents an arbitrary volume, $\boldsymbol{l} = (x, y)$ and $\boldsymbol{k}_\parallel$ labels the wavevector part associated to $E_\parallel = \hbar^2 k_\parallel^2/2m$. This procedure leads to

$$\begin{aligned} \psi_I(z) &= \exp(\mathrm{i}k_I z) + \left\{ \frac{\mathrm{i}k_I + k_{II}}{\mathrm{i}k_I - k_{II}} \right\} \exp(-\mathrm{i}k_I z), \qquad (z < 0), \\ \psi_{II}(z) &= \left\{ \frac{\mathrm{i}2k_I}{\mathrm{i}k_I - k_{II}} \right\} \exp(-k_{II} z) \qquad (z > 0), \end{aligned} \tag{24}$$

with

$$k_I = \left\{ \frac{2mE_\perp}{\hbar^2} \right\}^{1/2}, \qquad k_{II} = \left\{ \frac{2m(V_0 - E_\perp)}{\hbar^2} \right\}^{1/2}. \tag{25}$$

$\psi_{II}(z)$ is the permanent and *probabilistic* near-field component of the electronic wavefunction associated with the FESA electrons. This *scalar* near-field tails off the metal exponentially with a maximun inverse decay length

$$\eta = \frac{\sqrt{2m\phi}}{\hbar}. \tag{26}$$

Typically, for a metal work function $\phi = 4.5$ eV and $\eta = 1.08$ Å$^{-1}$. This is slightly smaller than the inverse decay of the electrostatic permanent near-field of the (100) NaCl surface (see section 2.1). The exponential nature of the evanescent wavefunction provides the opportunity for a uniquely sensitive form of microscopy (see figure 7). Exploitation of this simple electronic decay law began with the invention of the STM by Binnig and Rohrer in 1981. Since then, exploitation of this effect has enabled many original studies at subnanoscale resolution to be achieved (Descouts and Siegenthaler 1992). This kind of permanent near-field is not very sensitive to temperature and is essentially governed by the local work function along the surface (Behm *et al* 1990).

Note that the total charge density near the interface can be deduced from (23)–(25). Rigorously, we have

$$\rho(\boldsymbol{r}) = 2e \sum_k |\Psi(\boldsymbol{r})|^2 f(E(k)), \tag{27}$$

where $f(E(k))$ represents the Fermi–Dirac distribution. The charge density outside the metal turns out to be a sum of individual evanescent waves whose decay length $\eta^{-1}$ ranges from zero (for grazing incident electrons) to a maximun value $\eta_{\max}^{-1} = \hbar/2\sqrt{2m\phi}$ depending only on the metal work function. Consequently, the charge density that tails off the metal always behaves exponentially.

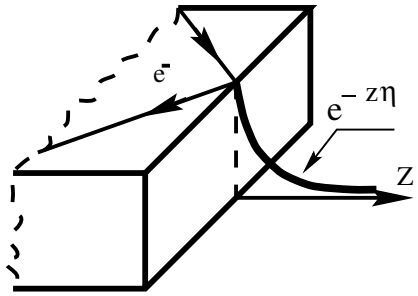


**Figure 7.** A particular evanescent wavefunction generated by an electron impinging specularly on the surface barrier.

In the absence of any approximation, equation (27) can be elaborated further by rearrangement, leading to

$$\rho(\boldsymbol{r}) = \frac{eK_BT}{\pi^2(E_F+\phi)}\int_0^{+\infty} \exp[-(2mV_0/\hbar^2 - k_I)^{1/2}z]\mathrm{Log}\left\{\frac{\exp(U/K_BT)+1}{\exp(U/K_BT)}\right\}k_I^2\,\mathrm{d}k_I \tag{28}$$

with $U = \frac{\hbar^2 k_I^2}{2m} - E_F$. This equation contains as asymptotic case the simple exponential law $\mathrm{e}^{-z\eta}$ associated with the Fermi-level electrons. Near the free surface of a metal the decay length $\eta^{-1}$ depends completely on the Fermi energy. It is technologically difficult to modify or to modulate this parameter from inside the metal.

## 3. Intrinsic properties of the near-fields

As detailed in section 2, the surface decay laws yield the first important information about the nature of the near-field under consideration. From the experimental point of view, these simple properties are essential to define a more efficient regulation method able to easily control the distance between the sample and the local near-field detector. Actually, simultaneous knowledge of the behaviour of different near-fields can be exploited to develop mixed experimental configurations in which gap-width control can be based on the detection of a physical observable different from the surface near-field under study (Betzig *et al* 1992, van Hulst *et al* 1993, Koglin *et al* 1997). The data gathered in table 1 gives a general idea of what happens when the observation point $\boldsymbol{R}$ gradually moves away from the surface. Obviously, this information can only be considered complete when we deal with idealized plane samples. In real situations, we have to account for the *lateral near-field variations* generated by the surface corrugations. As might be expected, all the wealth of the *near-field physics phenomena* is encoded in these lateral variations. Depending on the sample preparation, the surface corrugations can display different features ranging from the atomic scale to the micrometric scale. For each kind of surface near-field (electronic, photonic, ...), the lateral surface profile (also called surface topography) produces well defined near-field patterns. In particular, when the near-field is generated by particles (electrons or photons) of incident wavelength $\lambda$ that impinge on a sample displaying periodic surface structures or supporting some specific eigenmodes (see, for example, the quantum coral experiment by D Eigler (Crommie *et al* 1993)), the resulting patterns appear to be extremely sensitive to the relation between incident wavelength and structure spacing (Crommie *et al* 1993, Li *et al* 1998, Crampin and Bryant 1996). For example, in the case of illumination of pseudo-periodic surface structures by a monochromatic light beam, the excitation of local photonic states can generate specific near-field patterns (Girard *et al* 1995, Weeber *et al* 1996), as well as dramatic enhancement phenomena occurring in the near-field zone (Martin

**Table 1.** Comparative presentation of different near-field decay laws.

| | Near-field | | | |
|---|---|---|---|---|
| | Electrostatic fields (ionic crystals) | Optical surface evanescent waves | Mean square fluctuating near-fields | Electronic wavefunction (metal) |
| Decay law | exponential $\exp(-R\eta)$ | exponential $\exp(-R\eta)$ | $R^{-n}$ $(n = 3, 4, \ldots)$ | exponential $\exp(-R\eta)$ |
| Typical decay length $\eta^{-1}$ (Å) | $\simeq$0.6 | $\simeq$2000 | $\simeq$1000 | $\simeq$0.45 |

*et al* 1999). In this section, we discuss various peculiar near-field effects generated by well defined surface corrugation. Two examples borrowed from the near-field literature will be reviewed.

### *3.1. Optical near-field patterns generated by surface structures*

When an optical electromagnetic wave interacts with a localized surface defect, the electromagnetic energy distribution observed around the surface defect is extremely sensitive both to the illumination mode and the physical parameters of the defect (shape, optical index and size relative to the wavelength) (Celli *et al* 1975, Toigo *et al* 1977). A detailed understanding of this optical interaction between subwavelength structures and external light sources indisputably represents one of the most serious challenges raised by the tremendous recent experimental progress of NFO (Pohl and Courjon 1993).

Accurate description of the optical field distribution, prior to its local detection, is mandatory for describing properly the image formation mechanisms in NFO (Marti and Möller 1995). The main difficulties in achieving this goal are inherent in the complexity of the geometries investigated in NFO (non-periodic objects, localized surface defects, nanometre-size holes, ...) as well as in the need to account for a large spectra of non-radiative optical field components. In particular, corners, sharp edges and angular regions much smaller than the incident wavelength generate specific difficulties for most of the theoretical schemes and numerical methods for solving Maxwell's equations (Girard and Dereux 1996, Greffet and Carminati 1997) are needed. In the last three years, numerous simulations have been proposed. These simulations clearly show the different roles played by both *electric* and *magnetic* fields in the near-zone. They indicate unambiguously that the individual structures lying on the surface distort the optical near-field intensities established by the self-consistent interaction between the surface roughness and the incident light. In particular, it was demonstrated that when the lateral dimensions of tiny objects are significantly smaller than the incident wavelength, the interference pattern collapses and the optical electric near-field intensity distribution tends to be fairly well localized around the objects (see figure 8). Under well defined conditions for the incident field (polarization, wavelength) a highly localized electric near-field intensity occurs just above the subwavelength protrusions. Recently these considerations facilitated the interpretation of this peculiar NFO phenomenon. For example, a simple dielectric cube of cross section $100 \times 100$ nm$^2$ was imaged with the dielectric tip of a STOM/PSTM (photon STM) with a bright contrast when the surface wave was p polarized and with a dark contrast when it was s polarized.

In this section, we tackle this problem from a purely analytical point of view. In order to be consistent with the material in section 2.2, we continue the discussion in the TIR configuration

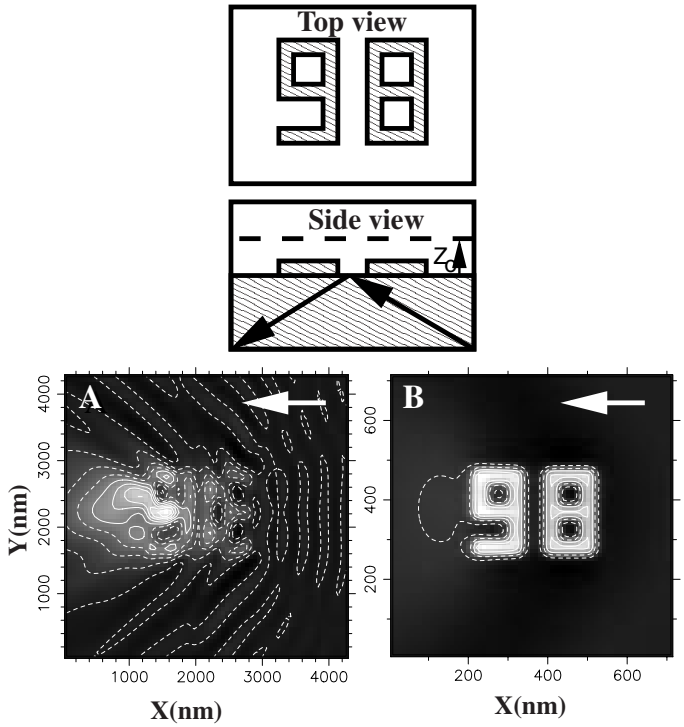


**Figure 8.** Illustration of the typical mesoscopic–nanometric transition occurring in NFO. The test object represents the number 98 nanolithographed on a silica surface. The two numerical simulations of the square electric field modulii are based on the *field-susceptibility/Green function theory* (incident wavelength $\lambda_0 = 633$ nm) (Girard and Dereux 1996). (*a*) The lateral size of the dielectric pattern are of the same magnitude order as the wavelength $\lambda_0$; (*b*) all the pattern dimensions have been reduced by a factor of 6. The two white arrows indicate the surface wave propagation direction.

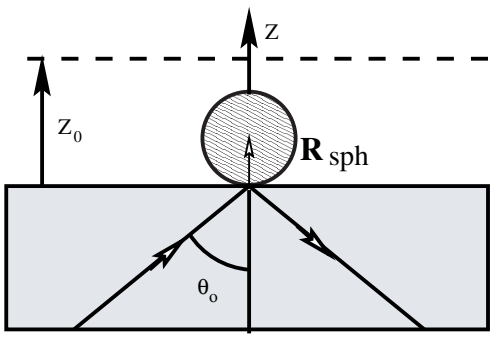


**Figure 9.** Schematic drawing of the model system used to treat the simplest form of surface corrugation. A transparent substrate, of optical index $n = 1.5$, supports a small dielectric sphere of diameter $D$. The system is illuminated in TIR with an incident angle $\theta_0$ and $\boldsymbol{R}_{\text{sph}} = (0, 0, D/2)$.

(see figure 2). To illustrate the coupling effect between an OEW and a small spherical object lying on a given sample, we consider the model system described in figure 9. The geometrical parameters used in this calculation are reported in the figure caption. The substrate modifies the polarizability $\alpha_0(\omega)$ of the particle. We then have

$$\alpha^{ef}(\boldsymbol{R}_{\text{sph}}, \omega) = \alpha_0(\omega) \cdot \boldsymbol{M}(\boldsymbol{R}_{\text{sph}}, \omega) \tag{29}$$

with

$$\boldsymbol{M}(\boldsymbol{R}_{\rm sph},\omega)=[\boldsymbol{I}-\boldsymbol{S}(\boldsymbol{R}_{\rm sph},\boldsymbol{R}_{\rm sph},\omega)\cdot\alpha_0(\omega)]^{-1} \tag{30}$$

where $\boldsymbol{S}(\boldsymbol{R}_{\rm sph},\boldsymbol{R}_{\rm sph},\omega)$ is the nonretarded propagator associated with the bare surface, and $\boldsymbol{R}_{\rm sph}=(0,0,D/2)$ labels the particle location. Within this description, the optical properties of the spherical particle–surface supersystem are described in terms of 'dressed' polarizability. In the past, several theoretical works (Metiu 1984) have been devoted to such calculation with molecular systems interacting with simple substrates (spheres, cylinders, planes, ...). If the particle polarizability $\alpha_0(\omega)$ is initially isotropic, the symmetry of the tensor $\alpha^{ef}(\boldsymbol{R}_{\rm sph},\omega)$ is governed mainly by the symmetry of the substrate. In the particular case of a single spherical particle interacting with a perfectly planar surface, the dyadic tensor $\boldsymbol{M}(\boldsymbol{R}_{\rm sph},\omega)$ becomes diagonal and, consequently, $\alpha^{ef}(\boldsymbol{R}_{\rm sph},\omega)$ belongs to the $C_{\infty v}$ symmetry group. In this case, $\alpha^{ef}$ may be described by two independent components $\alpha_{\|}^{ef}$ and $\alpha_{\perp}^{ef}$ (Metiu 1984, Girard and Dereux 1996, Keller 1996):

$$\alpha^{ef}(\boldsymbol{R}_{\rm sph},\omega)=\begin{pmatrix}\alpha_{\|}^{ef}(\boldsymbol{R}_{\rm sph},\omega) & 0 & 0\\ 0 & \alpha_{\|}^{ef}(\boldsymbol{R}_{\rm sph},\omega) & 0\\ 0 & 0 & \alpha_{\perp}^{ef}(\boldsymbol{R}_{\rm sph},\omega)\end{pmatrix} \tag{31}$$

with

$$\alpha_{\|}^{ef}(\boldsymbol{R}_{\rm sph},\omega)=\frac{8\alpha_0(\omega)D^3}{8D^3-\alpha_0(\omega)\Delta(\omega)} \tag{32}$$

and

$$\alpha_{\perp}^{ef}(\boldsymbol{R}_{\rm sph},\omega)=\frac{4\alpha_0(\omega)D^3}{4D^3-\alpha_0(\omega)\Delta(\omega)}. \tag{33}$$

In these two relations, the factor $\Delta(\omega)=\frac{(\epsilon(\omega)-1)}{(\epsilon(\omega)+1)}$ is merely the nonretarded reflection coefficient of the surface. Note that when working with two dielectric materials of low optical indices, the anisotropic ratio defined by

$$\xi=\frac{\alpha_{\perp}^{ef}}{\alpha_{\|}^{ef}} \tag{34}$$

remains close to unity over all the optical spectrum. In this case, we can easily verify that the effective polarizability of the particle can be replaced by the polarizability of the free particle with an excellent approximation. This approximation is no longer valid when dealing with metallic objects for which all further calculations must be performed on the basis of equations (32) and (33).

At a point $\boldsymbol{r}$ located above the sample in immediate proximity to the particle, the incident homogeneous surface wave is locally distorted. In fact, the fluctuating dipole moment $\mu(\boldsymbol{R}_{\rm sph},\omega_0)=\alpha^{ef}(\boldsymbol{R}_{\rm sph},\omega_0)\cdot\boldsymbol{E}_0(\boldsymbol{R}_{\rm sph},t)$ induced inside the particle itself produces two additional contributions to the electromagnetic field. At the first Born approximation, we can write

$$\boldsymbol{E}(\boldsymbol{r},t)=\boldsymbol{E}_0(\boldsymbol{r},t)+\boldsymbol{S}_0(\boldsymbol{r},\boldsymbol{R}_{\rm sph})\cdot\alpha^{ef}(\boldsymbol{R}_{\rm sph},\omega_0)\cdot\boldsymbol{E}_0(\boldsymbol{R}_{\rm sph},t) \tag{35}$$

and

$$\boldsymbol{B}(\boldsymbol{r},t)=\boldsymbol{B}_0(\boldsymbol{r},t)+\boldsymbol{Q}_0(\boldsymbol{r},\boldsymbol{R}_{\rm sph},\omega_0)\cdot\alpha^{ef}(\boldsymbol{R}_{\rm sph},\omega_0)\cdot\boldsymbol{E}_0(\boldsymbol{R}_{\rm sph},t) \tag{36}$$

where the dyadic tensors $\boldsymbol{S}_0(\boldsymbol{r},\boldsymbol{R}_{\rm sph})$ and $\boldsymbol{Q}_0(\boldsymbol{r},\boldsymbol{R}_{\rm sph},\omega_0)$ are the two usual free-space propagators that describe how an arbitrary dipole radiates electromagnetic energy (Landau

**Table 2.** Contrast in the s polarized mode.

| Field intensity | $\theta_0$ dependence | Sign of ($\Xi$) | Predicted contrast | Corrugation decay law |
|---|---|---|---|---|
| Electric | negligible | negative | dark | $r^{-3}$ |
| Magnetic | weak | positive | bright | $r^{-2}$ |

and Lifshitz 1960a). In the near-field zone, i.e. when $|\boldsymbol{r} - \boldsymbol{R}_{\rm sph}| < \lambda_0 = 2\pi c/\omega_0$, they can be expressed by

$$\boldsymbol{S}_0(\boldsymbol{r}, \boldsymbol{R}_{\rm sph}) = \frac{3(\boldsymbol{r} - \boldsymbol{R}_{\rm sph})(\boldsymbol{r} - \boldsymbol{R}_{\rm sph}) - |\boldsymbol{r} - \boldsymbol{R}_{\rm sph}|^2 \boldsymbol{I}}{|\boldsymbol{r} - \boldsymbol{R}_{\rm sph}|^5} \tag{37}$$

and

$$\boldsymbol{Q}_0(\boldsymbol{r}, \boldsymbol{R}_{\rm sph}, \omega_0) = \frac{\mathrm{i}\omega_0}{c|\boldsymbol{r} - \boldsymbol{R}_{\rm sph}|^3} \begin{pmatrix} 0 & -(z-D) & y \\ z-D & 0 & -x \\ -y & x & 0 \end{pmatrix}. \tag{38}$$

Current experimental measurements provide us with many images in which the small surface protrusions generally appear with either dark or bright contrast, corresponding either to a smaller or a larger number of detected photons. From equations (35) and (36) we are able to derive four useful analytical expressions explicitly showing the dependence of the near-field intensity constrast with respect to the external parameters. This can be achieved by defining two dimensionless coefficients depending on the location of the observation point $\boldsymbol{r}$:

$$\Xi_e(\boldsymbol{r}) = \frac{|\boldsymbol{E}(\boldsymbol{r})|^2}{|\boldsymbol{E}_0(\boldsymbol{r})|^2} - 1 \tag{39}$$

and

$$\Xi_m(\boldsymbol{r}) = \frac{|\boldsymbol{B}(\boldsymbol{r})|^2}{|\boldsymbol{B}_0(\boldsymbol{r})|^2} - 1. \tag{40}$$

When the observation point (which could be physically materialized by a sharp probe) is located just on the top of the particle (i.e. when $\boldsymbol{r} = \boldsymbol{R}_0 = (0, 0, Z_0)$), both the sign and magnitude of these coefficients provide direct information on the light confinement phenomenon occurring around the single particle. These simple relations can be used to analyse both the electric and magnetic contrasts near subwavelength dielectric particles. For example, for the electric part we can write

$$\Xi_{e,s} = -\frac{2\alpha_\parallel}{(Z_0 - R)^3}\{1 + \mathrm{o}(|Z_0 - R|^6)\} \tag{41}$$

and

$$\Xi_{e,p} = \frac{2\alpha_\perp(n^2 \sin^2\theta_0 + 1)}{(n^2 \sin^2\theta_0 - 1)(Z_0 - R)^3}\{1 + \mathrm{o}(|Z_0 - R|^6)\}. \tag{42}$$

The main physical behaviours predicted by these relations as well as the two ones for the magnetic part are summarized in tables 2 and 3.

Some comments can be made about these results.

(i) The more impressive success provided by these simple relations concerns the contrast. Indeed, when dealing with subwavelength-sized localized objects, the contrast predicted by the simple dipolar model is found in excellent agreement with available experimental data on similar objects (Weeber *et al* 1996). Additionally, all physical behaviours gathered in tables 2 and 3 are in agreement with the outputs produced by sophisticated *ab initio* Maxwell's equation solvers.

**Table 3.** Same as in table 2 but for the p polarized mode.

| Field intensity | $\theta_0$ dependence | Sign of ($\Xi$) | Predicted contrast | Corrugation decay law |
|---|---|---|---|---|
| Electric | weak | positive | bright | $r^{-3}$ |
| Magnetic | strong | negative | dark | $r^{-2}$ |

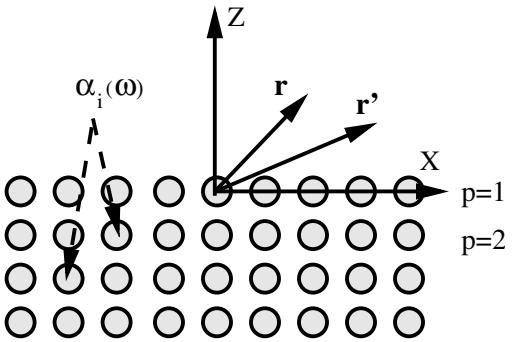


**Figure 10.** Schematic of a surface described as a set of polarizable centres $\alpha_i(\omega)$. In this simple model we consider that the solid is composed of an infinite number of atomic planes separated by a constant spacing $D$.

(ii) In the p polarized mode, equation (40) predicts subwavelength-sized magnetic field intensity patterns with a strong and dark contrast that dramatically depends on the incident illumination angle $\theta_0$. Although the complete angular investigation of this peculiar effect has not been yet realized, these trends seem to be in qualitative agreement with recent local measurements performed with metallic coated tips.

Before closing this discussion, let us note that other alternative methods lead to similar conclusions. In particular, the reciprocal-space perturbative approach based on Rayleigh approximation confirms this analysis (Barchiesi *et al* 1996).

### *3.2. Fluctuating near-field variation induced by surface corrugation*

As illustrated in the previous section, the surface topography variations affect the intrinsic structure of the near-fields. Consequently, in the presence of such surface features, the spontaneous fluctuating field described in section 2.3 loses a part of its lateral invariance properties and presents specific localized distortions. From a fundamental point of view, the proper description of this effect involves including in the general relation (18) a relevant form of *field susceptibility* $\boldsymbol{S}(\boldsymbol{r}, \boldsymbol{r}', \omega)$ able to account for surface corrugation. This quantity can be split into two contributions describing both the continuous and the corrugation part associated with the sample:

$$\boldsymbol{S}(\boldsymbol{r}, \boldsymbol{r}', \omega) = \overline{\boldsymbol{S}}(\boldsymbol{r}, \boldsymbol{r}', \omega) + \tilde{\boldsymbol{S}}(\boldsymbol{r}, \boldsymbol{r}', \omega). \tag{43}$$

At this stage, different descriptions can be adopted. For example, atomic scale corrugation occurring near a well defined surface can be treated as a discrete distribution of polarizable centres (see figure 10). The simplest approximation consists of the evaluation of $\boldsymbol{S}(\boldsymbol{r}, \boldsymbol{r}', \omega)$ by assuming an additive law between each polarizable centres. This leads to

$$\boldsymbol{S}(\boldsymbol{r}, \boldsymbol{r}', \omega) = \sum_i \int_v \boldsymbol{S}_0(\boldsymbol{r}, \boldsymbol{r}'', \omega) \cdot \alpha_i(\omega) \cdot \boldsymbol{S}_0(\boldsymbol{r}'', \boldsymbol{r}', \omega) \delta(\boldsymbol{r}'' - \boldsymbol{r}_i)\, \mathrm{d}\boldsymbol{r}'' \tag{44}$$

where $\boldsymbol{r}_i$ represents the atom positions in the solid and $\boldsymbol{S}_0$ the vacuum dipolar propagator defined in (37). In each atomic plane (labelled by the subscript $p$) the periodic arrangement of

the atoms may be characterized by a set of translation vectors $\boldsymbol{r}_i \equiv r_{p,\alpha,\beta} = \alpha(A,0)+\beta(0,A)$, in which $A$, the surface lattice parameter, has already been defined in section 2.1. In the case of a perfect crystal, the relation (44) can be elaborated further by exploiting the translational invariance of the atomic planes parallel to the surface. This property can be expressed by a Fourier expansion of the Dirac distribution (Steele 1974)

$$\sum_i \delta(\boldsymbol{r}'' - \boldsymbol{r}_i) \equiv \sum_{p,\alpha,\beta} \delta(\boldsymbol{r}'' - \boldsymbol{r}_{p,\alpha,\beta}) = \frac{1}{A^2} \sum_p \delta(z'' - z_p) \sum_{\boldsymbol{g}} \exp(\mathrm{i}\boldsymbol{g}\cdot\boldsymbol{l}) \tag{45}$$

where $\boldsymbol{g}$ represents a surface reciprocal lattice vector (see section 2.1). After some algebraic manipulations based on the well known Weyl expansion (Agarwal 1975) of the vacuum dipolar propagator $\boldsymbol{S}_0$ and on the assumption that the atoms are all defined with the same dynamical polarizability $\alpha(\omega)$, we obtain the following relation:

$$\boldsymbol{S}(\boldsymbol{r},\boldsymbol{r}',\omega) = \frac{\alpha(\omega)}{A^2} \sum_{p,\boldsymbol{g}} \int \mathcal{P}(\boldsymbol{k},\boldsymbol{g}) \mathrm{e}^{-\mathrm{i}\boldsymbol{k}\cdot\boldsymbol{l}} \mathrm{e}^{-\mathrm{i}\boldsymbol{k}_g\cdot\boldsymbol{l}'}\, \mathrm{d}\boldsymbol{k} \tag{46}$$

where the function $\mathcal{P}(\boldsymbol{k},\boldsymbol{g})$ is given by

$$\mathcal{P}(\boldsymbol{k},\boldsymbol{g}) = \frac{\mathcal{K}\cdot\mathcal{K}_g^\star \mathcal{K}\mathcal{K}_g^\star}{k|\boldsymbol{k}+\boldsymbol{g}|} \mathrm{e}^{-k(z-z_p)} \mathrm{e}^{-k_g(z'-z_p)}, \tag{47}$$

with $\boldsymbol{k}_g = \boldsymbol{k}+\boldsymbol{g}$, $\mathcal{K} = (\mathrm{i}\boldsymbol{k}, k)$, and $\mathcal{K}\boldsymbol{g} = (\mathrm{i}\boldsymbol{k}_g, k_g)$. Finally, as anticipated by equation (43), we can separate this relation into a continuous part ($\boldsymbol{g} = 0$) and a corrugation part ($\boldsymbol{g} \neq 0$). We find then two simple relations:

$$\overline{\boldsymbol{S}}(\boldsymbol{r},\boldsymbol{r}',\omega) = \frac{2\alpha(\omega)}{A^2} \sum_p \int \mathrm{d}\boldsymbol{k}\, \mathcal{K}\mathcal{K}^\star \mathrm{e}^{-\mathrm{i}\boldsymbol{k}\cdot(\boldsymbol{l}-\boldsymbol{l}')} \mathrm{e}^{-k(z+z'-2z_p)} \tag{48}$$

and

$$\tilde{\boldsymbol{S}}(\boldsymbol{r},\boldsymbol{r}',\omega) = \frac{2\alpha(\omega)}{A^2} \sum_{p,g_1>0,g_2\neq 0} \int \mathrm{d}\boldsymbol{k}\, \mathcal{P}(\boldsymbol{k},\boldsymbol{g}) \cos(\boldsymbol{k}_g\cdot\boldsymbol{l}' - \boldsymbol{k}\cdot\boldsymbol{l}) \tag{49}$$

where the dyadic character of these two response functions is accounted for by the juxtaposition of two vectors $\mathcal{K}$ and $\mathcal{K}_g$, or $\mathcal{K}^\star$ and $\mathcal{K}_g^\star$. It may be shown without formal difficulty that the continuous part $\overline{\boldsymbol{S}}$ is equivalent to the bulk expression (20) introduced in section 2.3 to materialize a perfectly planar sample. Indeed, in the asymptotic case where the atomic planes are assumed to be infinitely close, it is then possible to replace the sum over $p$ by an integral

$$\sum_p \Longrightarrow NA^2 \int_{-\infty}^{0} \mathrm{d}z_p \qquad \text{and} \qquad \alpha(\omega) \simeq \frac{\epsilon(\omega)-1}{4\pi N} \tag{50}$$

where $N$ and $\epsilon(\omega)$ are the atomic density and the local dielectric constant of the solid. By using these relations to elaborate equation (48) further, we recover the bulk expression (20). Therefore, the corrugation contribution (49) improves this result by introducing an additional structural term. According to the formalism exposed in section 2.3, we have now gathered all the ingredients needed to describe the effect of atomic surface corrugation on the spontaneous fluctuation field. Finally, substitution of (49) into (18) introduces a new contribution

$$\tilde{\mathcal{E}}(\boldsymbol{r},\boldsymbol{r}',\omega,\omega') = \frac{\hbar}{2\pi} \coth\left\{\frac{\hbar\omega}{2K_BT}\right\} \mathrm{Im}\,[\mathrm{Tr}\,\tilde{\boldsymbol{S}}(\boldsymbol{r},\boldsymbol{r}',\omega)]\delta(\omega+\omega'), \tag{51}$$

which gives

$$\tilde{\mathcal{E}}(\boldsymbol{R},\omega,\omega') = \frac{\hbar}{\pi A^2} \coth\left\{\frac{\hbar\omega}{2K_BT}\right\} \mathrm{Im}\,[\alpha(\omega)] \sum_{p,g_1>0,g_2\neq 0} \mathcal{F}(Z,\boldsymbol{g}) \cos(\boldsymbol{g}\cdot\boldsymbol{L})\delta(\omega+\omega'), \tag{52}$$

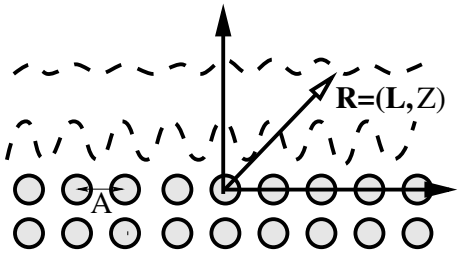


**Figure 11.** Schematic of the lateral variation of $\tilde{\mathcal{E}}(\boldsymbol{R})$ along a surface atomic row.

when the two observation points coincide (i.e. when $\boldsymbol{r} = \boldsymbol{r}' = \boldsymbol{R} = (\boldsymbol{L}, Z)$, see figure 11. For a given spatial harmonic $\boldsymbol{g} = \frac{2\pi}{A}(g_1, g_2)$ (see equation (5)), the function $\mathcal{F}(Z, \boldsymbol{g})$ occurring in relation (52) yields the decay rate of the corrugation part of the FNF. It may be shown that this quantity is proportional to a second-kind Bessel function $K_2$ of integer order (Abramowitz and Stegun 1970):

$$\mathcal{F}(Z, \boldsymbol{g}) = \frac{3\pi}{2(Z - z_p)^2} g^2 K_2[g(Z - z_p)]. \tag{53}$$

Outside of the electronic cloud zone of the surface atoms, the function $\mathcal{F}(Z, \boldsymbol{g})$ tends to adopt an exponential form with respect to the observation distance $Z$:

$$\mathcal{F}(Z, \boldsymbol{g}) \simeq \frac{3\pi^{\frac{3}{2}}}{2(Z - z_p)^{\frac{5}{2}}} \mathrm{e}^{-g(Z - z_p)}. \tag{54}$$

In consequence, the two first major contributions to equation (52) (i.e. when $(g_1, g_2) = (1, 0)$ or (0,1)) yield a maximun corrugation decay length $\eta^{-1} = A/2\pi$ proportional to the surface lattice parameter. In addition, equation (52) clearly indicates, through the modulation factor $\cos(\boldsymbol{g}\cdot\boldsymbol{L})$, a perfect commensurability between the surface atomic array and the lateral variation of the electromagnetic FNF. Actually, this important property remains valid for a large wavelength range $\lambda_{\mathrm{fluc}} = \omega/c$ of fluctuating fields for which

$$\lambda_{\mathrm{fluc}} \gg A \tag{55}$$

and, as will be shown later, this singular property is at the origin of the simple image–object relation in van der Waals atomic force microscopy.

At this stage an important comparison with another physical situation may be made. In fact, a similar behaviour in which the optical near-field pattern resembles the surface topography has already been predicted (Marti and Möller 1995) and observed in NFO (Weeber *et al* 1996). In the precise case of NFO, this phenomenon can occur only if the two following conditions are satisfied simultaneously (these conditions correspond to the case of figure 8(*b*)):

(i) The surface structures must display *subwavelength lateral size*. It was indeed demonstrated that when the lateral dimensions of tiny objects are significantly smaller than the incident wavelength, the interference pattern collapses and the optical electric near-field intensity distribution tends to be fairly well localized around the objects.
(ii) The polarization state of the incident light must be chosen so that the excitation electric field is perpendicular to the surface of the sample.

## 4. Detection and observation of the near-field

### *4.1. General concepts*

After inspection of the principal near-field properties, we turn to the crucial problem of local detection. Basically, the detection process is made possible thanks to a fundamental principle

**Table 4.** Some examples illustrating the relationship between physical near-field and detected physical quantity.

| | Surface near-field | | | |
|---|---|---|---|---|
| | Electrostatic near-field $\boldsymbol{E}$ | Optical surface evanescent field $\{\boldsymbol{E}; \boldsymbol{B}\}$ | Mean square fluctuating near-fields $\mathcal{E}$ | Electronic wave function at metal $\psi(\boldsymbol{r})$ |
| Physical detected quantity | Force | Photon energy flow | Force | Electric current |
| Magnitude order | nN | $\sim 10^9$ Ph $s^{-1}$ | nN | nA |
| Experimental device | AFM | SNOM PSTM/STOM | Noncontact AFM | STM |

that may be stated as follows: *'When some external material body is introduced into the near-field zone the initial equilibrium state is changed'*. Following this equilibrium state breaking off, and depending on the nature of the near-field under consideration, two kinds of specific physical phenomena may be expected:

- In any case, a force will occur between the sample and the external physical probe. The influence of such forces during the STM acquisition stage was recognized from the beginning of STM but the first scientist who had the idea of evaluating and exploiting these forces for atomic surface imaging purposes was Gerd Binnig in 1985 (Binnig *et al* 1986, Rugar and Hansma 1990).
- Depending on the near-field detection device, the appearance of this local force may be accompagnied by a tiny particle flow (electrons or photons) passing through the junction formed by the tip apex and the sample (see table 4).

Historically, in the optical range, the first experiment of near-field detection was reported three centuries ago by Isaac Newton. In a renowned experiment, Newton demonstrated for the first time that the total reflection of a light beam could be frustated by approaching a second prism close to the first transparent sample. In this case, the beam intensity seems to be captured by the second material and decays exponentially on increase of the spacing between the two bodies. Today this strange phenomenon can be explained with classical Maxwell equations by applying standard boundary conditions over the two interacting surfaces. This so-called optical tunnelling effect as well as its relation with the above-mentioned Newton experiment are well described in a recent and pedagogical review by Courjon (Courjon and Bainier 1994). Finally, let us note that, independent of the advent and success of *scanning probe methods*, the optical tunnelling effect had already produced many other powerful applications in the spectroscopy of molecular layers (Chen *et al* 1976, Pettinger *et al* 1979) as well as in confocal microscopy of surface samples (Guerra 1990, Guerra *et al* 1993).

In solid state physics, the observation of electrons tunnelling through thin metal–insulator–metal barriers provide a second illustration of near-field detection performed without accurate control of the barrier width (Frenkel 1930, Esaki 1957, Giaever 1960, Solymar 1972, Gauthier and Joachim 1992). About 18 years ago, an important breakthrough was achieved by Binnig, Rohrer, Gerber and Weibel who proposed the first successful tunnelling experiment with an externally and reproducibly adjustable vacuum gap. This preliminary experiment opened the way for the first generation of local probe devices in which the near-field is locally converted

into one or several measurable quantities thanks to a sharp-pointed detector (Behm *et al* 1990).

Nowadays, the current local probe instrumentation gives access to a more and more accurate representation of the lateral variation of the different surface near-fields by performing ultimate reductions of the junction lateral size. This progress is accompanied by considerable improvement in the tip–sample distance control. This new generation of surface analysis tools forms the so-called LPBMs which provide us with a wealth of new opportunities for characterization and modification of small objects at the nanometre scale. Simultaneously with the rapid advances of experimental techniques, an increasing demand has been felt for understandings of the relationship between the different forms of near-fields localized at the surface of materials and the detected signals obtained by raster scanning accross the sample. With the emergence of such instrumentation mainly oriented towards high-resolution microscopy, the major question to be addressed was the key issue related to the image–object relation. Depending on the nature of the near-field under consideration, this question received more or less complete answers:

(i) For example, in NFO, the physical content of the images is still debated. In this precise case, the difficulty seems to originate from the specific nature of the detection process (Weeber 1996, Dereux *et al* 1998). Indeed, recent observations indicate that when the detector extremity is either completely or partially covered with a thin metallic coating, both theoretical modellings and experimental measurements supply NFO images that do not follow the expected optical electric near-field intensity.

(ii) In SFM, in spite of impressive progress in image simulations of ordered atomic surface (Shluger *et al* 1994, Shluger *et al* 1995, Tang *et al* 1998), some points remained unresolved. In particular, the recently achieved super-resolution in noncontact SFM mode is not completely assessed (Giessibl 1995, Giessibl 1997) and pertinent dynamical models are being developed (Aimé *et al* 1999).

(iii) Unlike what happens with other LPBMs, the STM instrumentation currently benefits from an excellent theoretical support being particularly efficient for adsorbate image recognition.

The main purpose of this section is to illustrate three different configurations based respectively on electronic, photonic and mechanical interactions, the fundamental mechanisms existing between unperturbed near-fields and detected signals.

### *4.2. Local detection in NFO*

Understanding the optical tip–sample interaction surely presented one of the most serious challenges at the beginning of NFO microscopy research and many different approaches have been devoted to this problem (Van Labeke and Barchiesi 1992, Van Labeke and Barchiesi 1993, Girard and Dereux 1996, Greffet and Carminati 1997). In this section, the problem of the local detection in NFO will be reviewed. We start with a simple pedagogical model based exclusively on analytical materials. In a second step, we give some indication of the possibility of implementing an operational three-dimensional numerical scheme.

*4.2.1. NFO interaction with a spherical detector.* The conversion of evanescent waves into propagating waves can be performed with a dielectric stylus placed in the vicinity of the surface of the sample (Reddick *et al* 1989, Vigoureux *et al* 1989). The most simple picture to mimic this situation consists of replacing the pointed detector by a single dielectric sphere of radius

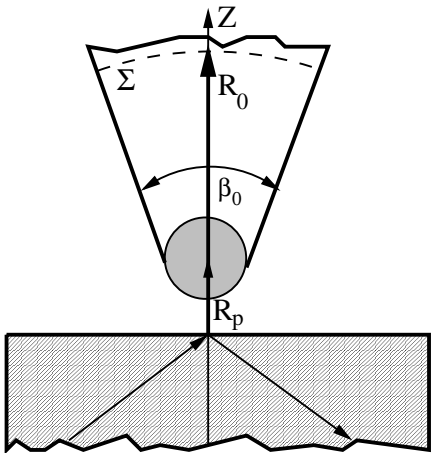


**Figure 12.** Geometry of a subwavelength spherical detector in interaction with the surface evanescent wave. The vector $\boldsymbol{R_p}$ refers the position of the spherical tip and the symbol $\Sigma$ represents a surface located in the 'wave zone' inside the upper part of the detector. The vector $\boldsymbol{R_o}$ defines the position of this surface with respect to the centre of the spherical tip and $\beta_0$ represents its aperture angle.

$a$ (see figure 12). When the tip is brought near the surface, it acquires a fluctuating dipole moment $\boldsymbol{m}_{\rm tip}(\boldsymbol{R_p}, t)$ proportional to the surface electric field. It is given by

$$\boldsymbol{m}_{\rm tip}(\boldsymbol{R_p}, t) = \alpha(\omega) \cdot \boldsymbol{E_o}(\boldsymbol{R_p}, \omega) \exp(\mathrm{i}\omega t) \tag{56}$$

where $\alpha(\omega)$ represents the dipolar polarizability of the spherical probe. This quantity can be expressed in terms of the optical dielectric constant $\epsilon_{\rm tip}(\omega)$ of the material

$$\alpha(\omega) = a^3 \left\{ \frac{\epsilon_{\rm tip}(\omega) - 1}{\epsilon_{\rm tip}(\omega) + 2} \right\}. \tag{57}$$

In turn, this fluctuating dipole scatters in the upper part of the tip a propagating wave of intensity proportional to†

$$I(\boldsymbol{R_p}) = \frac{\omega^2}{4\pi c^3} \int_\Omega \mathrm{d}\theta \, \mathrm{d}\phi \frac{\sin(\theta)}{R_0^2} [\boldsymbol{R}_0 \wedge \boldsymbol{m}_{\rm tip}(\boldsymbol{R_p}, \omega)]^2. \tag{58}$$

After performing integration over a conical aperture of angle $\beta_0$ (see figure 12), we find the following analytical expression:

$$I(\boldsymbol{R_p}, \beta_0) = I_1(\boldsymbol{R_p}, \beta_0) + I_2(\boldsymbol{R_p}, \beta_0). \tag{59}$$

The two contributions are given by (Landau and Lifshitz 1960a)

$$I_1(\boldsymbol{R_p}, \beta_0) = \frac{\omega^2}{2c^3} \left\{ \frac{2}{3}(1 - \cos^3(\beta_0))[m_{{\rm tip},x}^2 + m_{{\rm tip},y}^2] \right\} \tag{60}$$

and

$$I_2(\boldsymbol{R_p}, \beta_0) = \frac{\omega^2}{2c^3} \left( \frac{2}{3} - \frac{3}{4}\cos(\beta_0) + \frac{1}{12}\cos(3\beta_0) \right) [2m_{{\rm tip},z}^2 + m_{{\rm tip},x}^2 + m_{{\rm tip},y}^2]. \tag{61}$$

Two important limiting cases can be defined from these simple relations.

(i) The small aperture angle limit. In this particular case, the intensity becomes independent of the scattering dipole component perpendicular to the surface

$$I(\boldsymbol{R_p}) \sim \beta_0^2 [m_{{\rm tip},x}^2 + m_{{\rm tip},y}^2]. \tag{62}$$

Consequently, for a detector of very small aperture angle, the detection process could introduce a strong anisotropy able to mask some components of the vectorial near-field.

† In the NFO literature the fact of decoupling the probe from the sample corresponds to the *passive dipolar probe approximation* (Greffet and Carminati 1997).

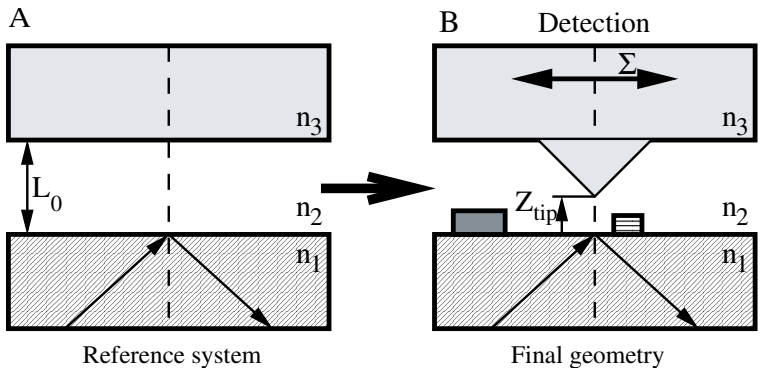


**Figure 13.** Schematic drawing illustrating how we can elaborate a realistic 3D model. (*a*) We start with a high-symmetry reference system composed of three dielectric media of optical index $n_1, n_2$ and $n_3$. (*b*) The symmetry is then lowered by introducing additional pieces of matter inside the gap. Some years ago, a similar construction was proposed by A Lucas to describe the detection process in STM.

(ii) The large aperture angle limit ($\beta_0 = \pi/2$)

$$I(\boldsymbol{R_p}) = \frac{2\omega^2}{3c^3}|\boldsymbol{m}_{\rm tip}(\boldsymbol{R_p}, \omega)|^2 \equiv \frac{2}{3}\left\{\frac{\omega\alpha A_0 T_s}{c}\right\}^2 {\rm e}^{-\eta R_p}, \qquad \text{(s-mode)}. \tag{63}$$

This simple relation clearly indicates that, within the *passive dipolar probe approximation*, the detected intensity can be considered as proportional to the near-field square. It may be applied to explain qualitatively many experimental situations.

Based on a simple model, these relations show explicitly the importance of the physical detector parameters to the spatial dependence of the intensity.

*4.2.2. Beyond the dipolar passive probe approximation.* The qualitative analysis previously exposed must be completed by a more realistic description able to properly account for both finite size effect and tip–sample coupling. Very recently, an original approach to this problem has been detailed in a work by Ward and Pendry. In their paper, these authors employed a *transfer matrix method* currently applied in the theory of photonic band gap. By using an adaptative coordinate transformation they were able to model realistic SNOM tip designs and to realize a comparative analysis of transmission efficiencies. This problem can be also tackled with a peculiar adaptation of the integral representation of Maxwell's equations (Girard and Courjon 1990, Dereux *et al* 1991, Dereux 1991, Dereux and Pohl 1993, Girard 1998). First we start from the known solutions associated with a simple planar optical junction formed by three dielectric media of optical indices $n_1$, $n_2$, and $n_3$ (with $n_1 > n_2$, see figure 13(*a*)). The complete electromagnetic state of this junction can be obtained after applying the standard boundary condition. Three quantities are needed to describe this initial state:

(i) the initial electric and magnetic fields $\{\boldsymbol{E}_0(\boldsymbol{r}, \omega), \boldsymbol{B}_0(\boldsymbol{r}, \omega)\}$;
(ii) the field susceptibility of the bare junction $S_0(\boldsymbol{r}, \boldsymbol{r}', \omega)$ (Agarwal 1975).

Now let us see how to evolve the initial electromagnetic state when a 3D microtip supported by the *output* medium is inserted in the gap (see figure 13(*b*)) together with some structures localized on the bearing sample ($n_1$). As previously demonstrated (Girard 1998), the new electromagnetic field state $\{\mathcal{E}(\boldsymbol{r}, \omega), \mathcal{B}(\boldsymbol{r}, \omega)\}$ can be derived everywhere in the junction by

introducing two generalized propagators labelled $\mathcal{K}(\boldsymbol{r}, \boldsymbol{r}', \omega)$ and $\mathcal{L}(\boldsymbol{r}, \boldsymbol{r}', \omega)$, respectively. If the whole junction responds linearly to the excitation, the electromagnetic field can be described by the two following linear relations:

$$\mathcal{E}(\boldsymbol{r}, \omega) = \int_v \mathcal{K}(\boldsymbol{r}, \boldsymbol{r}', \omega) \cdot \boldsymbol{E}_0(\boldsymbol{r}', \omega)\, \mathrm{d}\boldsymbol{r}', \tag{64}$$

and

$$\mathcal{B}(\boldsymbol{r}, \omega) = \int_v \mathcal{L}(\boldsymbol{r}, \boldsymbol{r}', \omega) \cdot \boldsymbol{E}_0(\boldsymbol{r}', \omega)\, \mathrm{d}\boldsymbol{r}' \tag{65}$$

where the integral runs over the volumes occupied by the microtip and the objects. The dyad $\mathcal{K}(\boldsymbol{r}, \boldsymbol{r}', \omega)$, also called the *generalized electric field propagator*, can be formulated in terms of the optical field susceptibility tensor $\mathcal{S}(\boldsymbol{r}, \boldsymbol{r}', \omega)$ associated with the entire system described by figure 13(*b*):

$$\mathcal{K}(\boldsymbol{r}, \boldsymbol{r}', \omega) = \delta(\boldsymbol{r} - \boldsymbol{r}') + \mathcal{S}(\boldsymbol{r}, \boldsymbol{r}', \omega) \cdot [\chi_{\mathrm{tip}}(\boldsymbol{r}', \omega) + \chi_{\mathrm{obj}}(\boldsymbol{r}', \omega)] \tag{66}$$

where $\chi_{\mathrm{tip}}$ and $\chi_{\mathrm{obj}}$ are the linear electric susceptibilities of the microtip and the object located in the gap. The second propagator $\mathcal{L}(\boldsymbol{r}, \boldsymbol{r}', \omega)$ establishes a direct relation between incident electric field and local magnetic field. When dealing with nonmagnetic materials it may be expressed as a functional of $\mathcal{K}(\boldsymbol{r}, \boldsymbol{r}', \omega)$:

$$\mathcal{L}(\boldsymbol{r}, \boldsymbol{r}', \omega) = \frac{\delta(\boldsymbol{r} - \boldsymbol{r}')}{\mathrm{i}k_0}\Lambda_{\boldsymbol{r}'} + \int_v \boldsymbol{Q}_0(\boldsymbol{r}, \boldsymbol{r}'', \omega) \cdot [\chi_{\mathrm{tip}}(\boldsymbol{r}'', \omega) + \chi_{\mathrm{obj}}(\boldsymbol{r}'', \omega)] \times \mathcal{K}(\boldsymbol{r}'', \boldsymbol{r}', \omega)\, \mathrm{d}\boldsymbol{r}'' \tag{67}$$

where $\Lambda_{\boldsymbol{r}'}$ labels the matrix form of the *curl* operator and $\boldsymbol{Q}_0(\boldsymbol{r}, \boldsymbol{r}', \omega)$ represents the so–called *electric–magnetic mixed susceptibility* of the bare junction (Girard 1998). After a solving procedure of (64) and (65) based on a recursive algorithm of Dyson's equation associated to $\mathcal{S}$, we can generate the electromagnetic field $\{\mathcal{E}(\boldsymbol{r}, \omega), \mathcal{B}(\boldsymbol{r}, \omega)\}$ everywhere in the system. The time-average Poynting vector field at the exit of the device is then defined by

$$\mathcal{P}(\boldsymbol{r}) = \tfrac{1}{2}\mathrm{Re}\,\{\mathcal{E}(\boldsymbol{r}, \omega) \wedge \mathcal{B}^*(\boldsymbol{r}, \omega)\}. \tag{68}$$

Finally, from the information contained in (68), we are able to define a transmission coefficient characterizing the optical transparence of the device. This quantity will be normalized with respect to the incident energy $E_{\mathrm{inc}}$ crossing a surface $\Sigma$ located inside the input medium and centred around the microtip (see figure 13(*b*)):

$$T(Z_0, \theta_0, \lambda) = \frac{\int_\Sigma \mathcal{P}(\boldsymbol{l}, Z_0 + Z_\Sigma) \cdot \boldsymbol{u}_z\, \mathrm{d}\boldsymbol{l}}{E_{\mathrm{inc}}} \tag{69}$$

where $Z_\Sigma$ defined the location of the surface $\Sigma$ in the *output* medium of the exit medium, $\boldsymbol{l} = (x, y)$ and $\boldsymbol{u}_z$ is a unit vector directed along the $OZ$ axis. The numerical method described above is now sufficiently mature to faithfully reproduce different experimental processes at work in real experiments (imaging, local spectroscopy, optical binding forces, ...). In particular, the possibility of including the 3D character of the devices simultaneously with a description of their photonic energy transfer, constitutes a significant advance on previous numerical frameworks.

### *4.3. Tunnel current detection in STM*

For several years, because of the growing success of the STM, this phenomenon has been extensively discussed in the literature (Tsukada *et al* 1991b, Güntherodt and Wiesendanger 1993, Güntherodt and Wiesendanger 1994). Consequently, we limit ourselves to some

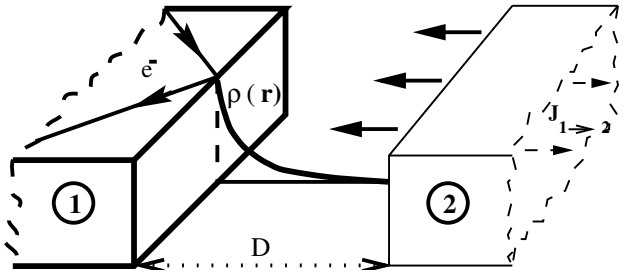


**Figure 14.** Schematic drawing illustrating the progressive approach of two planar metal interfaces.

fundamental aspects that concern the physical mechanisms governing the conversion of a *permanent electronic surface charge density* into a *direct tunnel electron current* resulting from the transfer of electrons from one electrode to another electrode.

*4.3.1. The planar model.* To illustrate the STM conversion process, we start with the usual planar junction configuration depicted in figure 14. In fact, when the second material significantly enters the near-field zone of the first metal, in the same way as a photon flow occurs in Newton's prism experiment, an electronic current can be expected in the circuit. At zero bias voltage, the average number of electrons transferred from *left to right* and from *right to left* is identical and, consequently, the net electronic current $I(D)$ passing through the junction is zero. In fact, in order to generate a permanent measurable current, a macroscopic voltage $V_0$ (see figure 15) must be applied to the device (Giaever 1974, Binnig and Rohrer 1982, Binnig *et al* 1984). The net current per unit area is given by the well known relation (Duke 1969)

$$I(D, V_0) = \boldsymbol{J}_{1\to 2}(D, V_0) - \boldsymbol{J}_{2\to 1}(D, V_0), \tag{70}$$

with

$$\boldsymbol{J}_{1\to 2}(D, V_0) = \frac{e}{4\pi^3}\iiint \mathrm{d}k_z\,\mathrm{d}\boldsymbol{k}_\parallel \frac{1}{\hbar}\frac{\partial}{\partial k_z} T_{1\to 2}(E_z, V_0, D) f_1(E)(1 - f_2(E + V_0)), \tag{71}$$

and

$$\boldsymbol{J}_{2\to 1}(D, V_0) = \frac{e}{4\pi^3}\iiint \mathrm{d}k_z\,\mathrm{d}\boldsymbol{k}_\parallel \frac{1}{\hbar}\frac{\partial}{\partial k_z} T_{2\to 1}(E_z, V_0, D) f_2(E + V_0)(1 - f_1(E)), \tag{72}$$

where $\boldsymbol{k}$ and $E$ represents both the wavevector and the energy of a given electron, $T_{1\to 2}$ and $T_{2\to 1}$ are the usual transmission coefficients and $f_{1/2}$ the Fermi–Dirac distributions of the two metals. A transparent introduction to the basic theoretical background prior to STM is also available in (Klein and Sacks 1992).

These relations characterize the tunnel properties of an idealized MVM planar junction. They can be used to reproduce the $I(V_0)$ characteristic: for small applied voltage, the $I(V_0)$ characteristic follows the usual linear law (see figure 16)

$$I(V_0) = \Upsilon V_0 \tag{73}$$

where the conductance $\Upsilon$ is proportional to the penetration coefficient $\exp[-2\eta D]$ associated with the charge density of the left electrode (labelled (1) in figure 15) (the inverse decay length factor $\eta$ has already been defined in section 2.4). Beyond this linear regime, the slope of the curve increases rapidly, to finally join the so-called Fowler and Nordheim electronic emission regime (Fowler and Nordheim 1928).

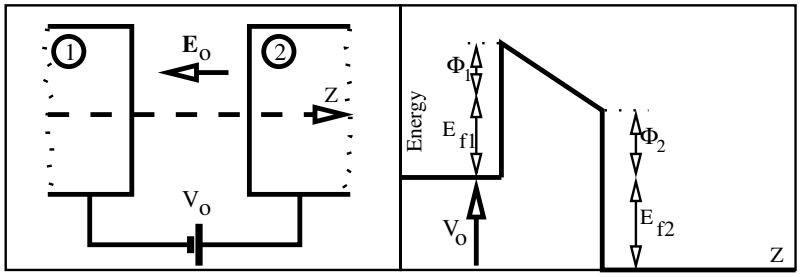


**Figure 15.** Typical potential energy curve occurring when the junction is biased by an external electric potential $V_0$. In this case the net current flows from left to right.

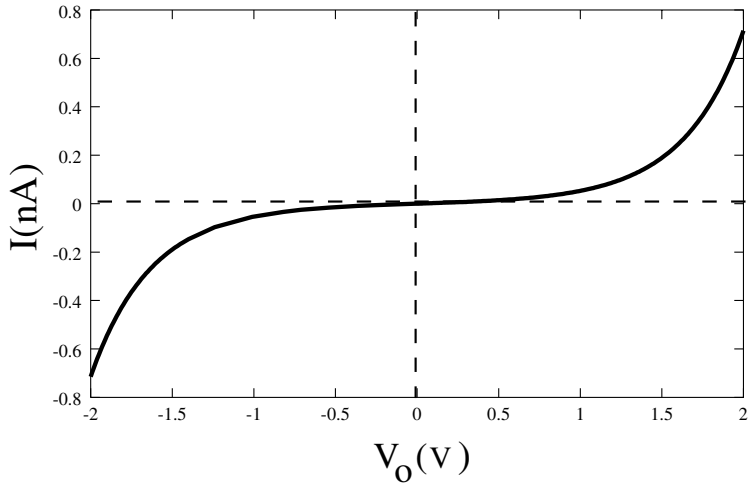


**Figure 16.** Typical current–voltage curve of a metal–$SiO_2$–metal planar tunnelling junction. These data come from the numerical implementation of the relations (70)–(72). $D = 3$ nm and both the work function and the facing areas are equal to 3.17 eV and 6.4 $\mu$m$^2$ respectively.

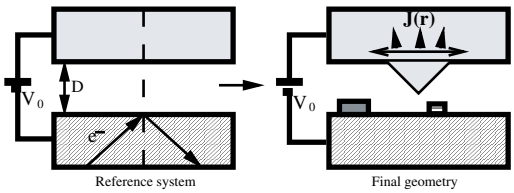


**Figure 17.** Schematic decomposition of the tunnel barrier into a planar and a localized part.

*4.3.2. Tunnelling through three-dimensional localized barrier.* Since the beginning of the 1980s, the growing need for both efficient and reliable numerical schemes able to guide and interpret actual STM measurements has led to different classes of three-dimensional models. The corresponding material was reviewed by Tsukada *et al* (1991b).

Among the different possibilities compatible with a relative low cost in terms of numerical implementation, the effective barrier scheme treated in the previous section 4.3.1, was extended by Lucas *et al* as early as 1988 to describe 3D models of tunnel junctions (Lucas *et al*

1988, Lucas 1990, Lucas *et al* 1994). In fact, the presence of a pointed metallic system placed in interaction with a sample displaying a corrugated surface (atomic or multi-atomic steps, terraces, ...) made the application of a standard boundary condition method difficult. To overcome this difficulty, Lucas proposed to start from the known solution of a highly symmetrical system, for example the pair of metallic plane electrodes considered in the previous section. The main ingredients associated with this simple geometry are both the electronic wavefunction $\Phi_0(\boldsymbol{r}, E)$ and the Green function $\mathcal{G}_0(\boldsymbol{r}, \boldsymbol{r}', E)$ of the reference system (see figure 17(*a*)). Note that these two quantities can be easily deduced from the simple formulation already evoked in section 4.3.1. For example, the relation between $\mathcal{G}_0(\boldsymbol{r}, \boldsymbol{r}', E)$ and the 1D Green function $G_{1D}(\boldsymbol{r}, \boldsymbol{r}', E)$ of the biased barrier is just given by the following Fourier transform:

$$\mathcal{G}_0(\boldsymbol{r}, \boldsymbol{r}', E) = \frac{1}{4\pi^2} \iint G_{1\mathrm{D}} \left( \boldsymbol{r}, \boldsymbol{r}', E - \frac{\hbar^2}{2m}(k_x^2 + k_y^2) \right) \times \exp[-\mathrm{i}(k_x(x - x') + k_y(y - y'))] \, \mathrm{d}k_x \, \mathrm{d}k_y. \tag{74}$$

In a second stage, similarly to what it was done in NFO (see section 4.2.2), additional materials can be introduced inside the bare reference system (for example, tip apex plus surface structures). The new electronic wavefunction $\Phi(\boldsymbol{r}, E)$ can then be computed self-consistently by introducing the generalized propagator $\Pi(\boldsymbol{r}, \boldsymbol{r}', E)$ associated to the complete junction (see figure 17(*b*)):

$$\Phi(\boldsymbol{r}, E) = \int \Pi(\boldsymbol{r}, \boldsymbol{r}', E) \Phi_0(\boldsymbol{r}', E) \, \mathrm{d}\boldsymbol{r}', \tag{75}$$

with

$$\Pi(\boldsymbol{r}, \boldsymbol{r}', E) = \delta(\boldsymbol{r} - \boldsymbol{r}') + \int \mathcal{G}(\boldsymbol{r}, \boldsymbol{r}', E) \Delta V(\boldsymbol{r}') \, \mathrm{d}\boldsymbol{r}', \tag{76}$$

where $\Delta V$ represents the variation of the potential barrier when passing from the bare reference system to the actual system as schematized in figure 17. The response function $\mathcal{G}(\boldsymbol{r}, \boldsymbol{r}', E)$ defines the 3D electronic Green function of the complete junction. It verifies the Dyson equation:

$$\mathcal{G}(\boldsymbol{r}, \boldsymbol{r}', E) = \mathcal{G}_0(\boldsymbol{r}, \boldsymbol{r}', E) + \int \mathcal{G}_0(\boldsymbol{r}, \boldsymbol{r}'', E) \Delta V(\boldsymbol{r}'') \mathcal{G}(\boldsymbol{r}'', \boldsymbol{r}', E) \, \mathrm{d}\boldsymbol{r}''. \tag{77}$$

In complete analogy with the standard procedure applied to solve the tunnel effect with photons (see section 4.2.2), this equation can be handled with powerful recursive algorithms (Martin *et al* 1995, Pendry *et al* 1991). The ability of this procedure to deal with large surface structures is, of course, a fundamental advantage when studying the physical interaction between biased STM tips and corrugated surfaces. Such an algorithm avoids the numerical inversion of a very large matrix ($3N \times 3N$) (where $N$ is the total number of discretization cells located inside the bare reference system) by reducing the self-consistent problem into a succession of ($3 \times 3$) matrix inversions. This iterative scheme is therefore relevant for all studies concerned with a great number of degrees of freedom because it is much less critical in terms of numerical stability. It is particularly well suited for considering low-symmetry systems for which first-principle calculations can rapidly become intractable.

After solving equations (75)–(77), we can generate the electronic wavefunction everywhere in the junction. The current density distribution is then given by the standard relation (given for $T = 0$):

$$\boldsymbol{J}(\boldsymbol{r}) = \int \mathrm{d}E \int \mathrm{d}\boldsymbol{k} (\Phi^\star(\boldsymbol{r}, E) \nabla \Phi(\boldsymbol{r}, E) - (\Phi(\boldsymbol{r}, E) \nabla \Phi^\star(\boldsymbol{r}, E)) \tag{78}$$

where the first integral must be performed on the energy range $E_f - V_0 \leqslant E \leqslant E_f$, and the second one on all incoming electronic waves directed towards the barrier (Lucas *et al* 1992). As expected, such an idealized model, essentially based on the concept of local effective barrier, is not able to reproduce all the complex situations encountered in most STM experiments (localized electronic state effects, atomic corrugations, chemical specificity of adsorbed molecules). Nevertheless, it may be a valuable tool if we want to couple in a simple way the tunnel current with others physical quantities (force, tip–sample optical excitation, ...).

*4.3.3. More realistic descriptions based on atomic descriptions of the junction.* As already mentioned, unlike what happens with electromagnetic fields for which incident wavelengths are much larger than atomic spacings in materials, a continuous barrier model cannot describe fully the different aspects of the detection mechanism in STM (Stoll 1984, Baratoff 1984, Stoll *et al* 1984, Sacks *et al* 1987, Lucas *et al* 1992). For this reason, many physicists developed alternative methods that rely on atom-by-atom description of the surface, tip and adsorbates (Tersoff and Hamann 1985, Tekman and Ciraci 1989, Tsukada *et al* 1991a, Sautet and Joachim 1991, Chavy *et al* 1993, Joachim *et al* 1992, Joachim *et al* 1995), or at least of the adorbates (Lang 1986, Lang 1994).

Among these different approaches, the ESQC technique developed as early as 1988 (Joachim 1988, Sautet and Joachim 1988) appears to be particularly well suited to treating the challenging problem of electron tunnelling through adsorbates ranging from simple adatoms to complex molecules. In this context numerous systems have already been investigated:

(i) rare gas (Bouju *et al* 1993),
(ii) small molecules (Sautet and Joachim 1991, Sautet and Bocquet 1994, Sautet and Bocquet 1996),
(iii) large adsorbates (Sautet and Joachim 1992, Chavy *et al* 1993).

The ESQC method offers a means of studying the transmission of elastic electrons through a *localized defect* inserted in an infinite periodic medium. When first proposed (Sautet and Joachim 1988), the method was applied to the study of the transmission of electrons through a molecular switch. More recently, in 1991, the method was further developed so that it could allow the study of tunnelling electrons in STM. In this case, the *defect* consists of the apex of the STM tip, the adsorbate to be imaged and the surface atoms of the substrate (see figure 18). Within this quantum chemistry based method, the electronic structure of the tip apex junction is implemented with an appropriate *atomic orbital description* compatible with currently available computation resources (for example, by constructing an extended Hückel Hamiltonian with a double zeta basis set). The tunnelling current intensity can be then calculated within the ESQC approximation by applying the generalized Landauer formula (Landauer 1970):

$$I(V_0) = \frac{e^2}{\pi\hbar} T(E_f) \equiv \frac{e^2}{\pi\hbar} \mathrm{Tr}\{\mathcal{T}(E_f) \cdot \mathcal{T}^+(E_f)\} \tag{79}$$

where the multichannel transmission matrix $\mathcal{T}$ is calculated from a nonunitary transformation of the spatial propagator describing the scattering the Bloch waves on the STM junction. For large molecules, the matrix elements of this propagator are obtained from a Hamiltonian given by the extended Hückel molecular orbital method.

Let us emphasize that this real-space methodology can integrate other specific functionalities. For example, it makes it possible for the local mechanical deformation to be taken into account during the approach of the STM tip apex (Joachim *et al* 1995, Pizzagalli *et al* 1997, Pizzagalli *et al* 1998). To illustrate this aspect we present in figure 19 two scanlines

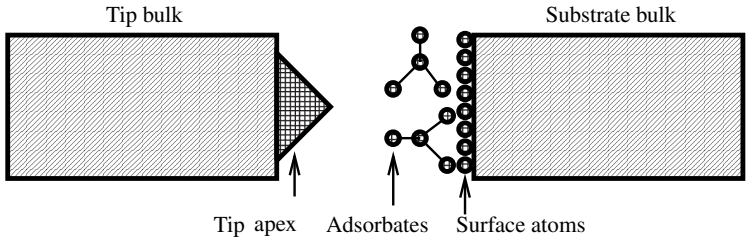


**Figure 18.** Schematic drawing illustrating the basics of the ESQC method.

computed above three Xe atoms adsorbed on the (110) face of copper. The weak tunnelling current $I$ passing through the tip apex–$Xe_3$–surface junction is calculated from the STM-ESQC technique. The tip apex is a cluster of ten copper atoms [111] oriented. This cluster is adsorbed on the (110) surface of the tip bulk. The other part of the junction is a Cu(110) surface supported by its bulk. The Xe electronic structure are described by their filled 5p and empty 6s atomic orbitals. These 5p orbitals are required to properly describe the $Xe_3$ molecular orbitals at small Xe–Xe distances when the Xe atoms are in close electronic interaction with the tip apex. Note that this result is found in fairly good agreement with experimental available data (Eigler and Schweizer 1990, Eigler *et al* 1991b). To conclude this important topic, we illustrate the ESQC capability with an example of realistic STM image computation of large molecules (constant current mode) (see figure 20). The modelled system consists of a single hexa-*tert*-butyl decacyclene (HB-DC) molecule adsorbed on a Cu(100) surface. Recently, experimental vizualisation of this molecular species was reported and similar six-lobed images were always observed if the molecules are blocked in the local molecular surroundings generated by other adsorbed molecules (Gimzewski *et al* 1998).

### *4.4. Conversion of FNF into measurable force field*

We close our enumeration of near-field detection phenomena by analysing further the physical mechanisms responsible for the conversion of spontaneous FNF into measurable force field. According to the content of section 3.2, we know that atomic surface structures are encoded in the lateral variation of the *mean square fluctuating field* $\mathcal{E}(\boldsymbol{r}', \boldsymbol{r}'', \omega', \omega'')$ calculated at a single position $\boldsymbol{R} = \boldsymbol{r}' = \boldsymbol{r}''$. Similarly to what happens with any other kind of near-field, we do not access to this information because of the evanescent behaviour of $\mathcal{E}$ when going far away from the sample. To be detected, this field must also be coupled with an additional element—the probe tip—introduced into the surface fluctuating field (see figure 21). Following the well known work by Lifschitz, it is well established that the force $\mathcal{F}(\boldsymbol{R})$ arising from this coupling is known as the van der Waals dispersion force. Let us examine how this force can be related to the surface fluctuation field $\mathcal{E}(\boldsymbol{R}, \omega', \omega'')$. Within a simplified picture† we can write that each infinitesimal element $\delta v$ located at a position $\boldsymbol{r}_t$ inside the tip acquires an additional energy induced by all fluctuating field components $(\omega', \omega'')$ (Mahanty and Ninham 1976)

$$\delta U(\boldsymbol{R} + \boldsymbol{r}_t) = -\tfrac{1}{2} \iint \exp \mathrm{i}(\omega' + \omega'')t \, \chi_{\mathrm{tip}}(\boldsymbol{r}_t, \omega') \cdot \mathcal{E}(\boldsymbol{R} + \boldsymbol{r}_t, \omega', \omega'') \, \mathrm{d}\omega' \, \mathrm{d}\omega'' \delta v \tag{80}$$

where $\chi_{\mathrm{tip}}(\boldsymbol{r}_t, \omega)$ represents the local electric susceptibility of the probe tip. In the case of a continuous description of the tip material, it is given in terms of the dielectric permittivity

† This approximation consists of neglecting the possible correlation between each element that composes the detector. In other words, the boundary conditions on the surface tip are not completely satisfied. This approximation might easily be removed by applying the fully self-consistent model described in Girard and Bouju (1991).

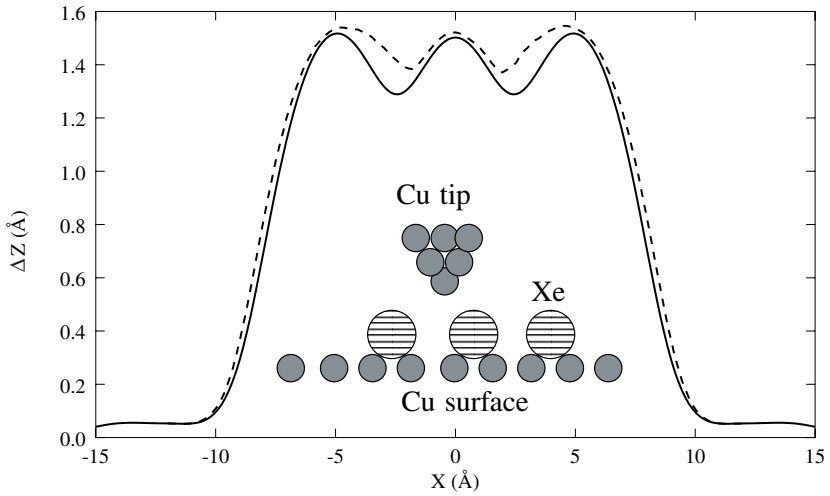


**Figure 19.** Scanlines computed above three Xenon atoms aligned along the [1,-1,0] row of Cu(110) surface. The calculation is performed at constant current and voltage ($I_{\mathrm{ref}} = 1$ nA and $V_0 = 10$ mV). Dashed curve: fully relaxed calculation; solid curve: same calculation, keeping frozen the adsorbate in the initial equilibrium configuration (from X Bouju, C Joachim and C Girard, unpublished results).

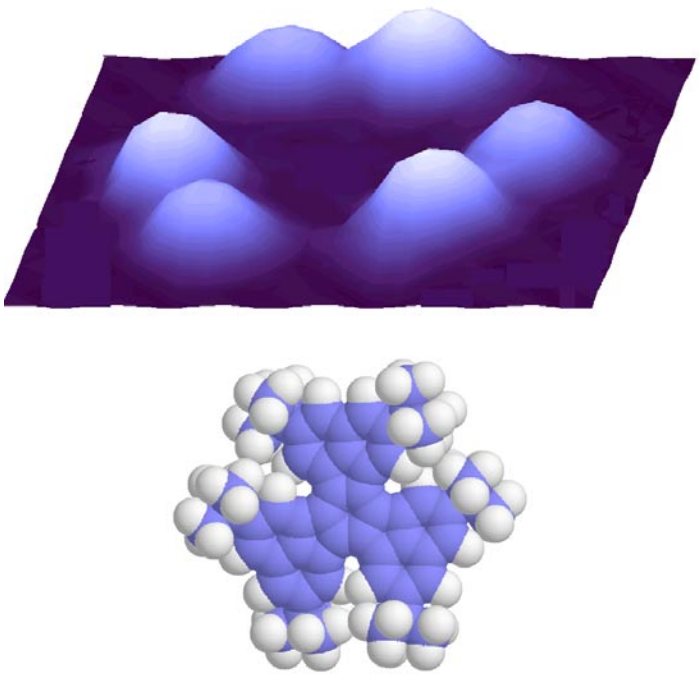

**Figure 20.** Example of an STM image calculated with the ESQC method. The molecule consists of a central conjugated decacyclene core with six *t*-butyl legs attached to its peripheral anthracene components. The molecule is supported by a Cu(100) surface. (Image courtesy of H Tang.)

(This figure is in colour only in the electronic version, see `www.iop.org`)

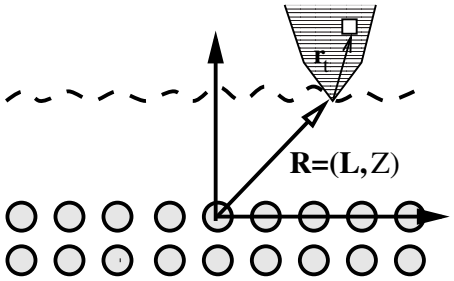


**Figure 21.** Basic geometrical arrangement for the calculation described in this section.

$\epsilon_{\rm tip}(\omega)$, i.e. $\chi_{\rm tip}(\boldsymbol{r}_t,\omega) = (\epsilon_{\rm tip}(\omega)-1)/4\pi$ for all points $\boldsymbol{r}_t$ located inside the tip, and $\chi_{\rm tip}(\boldsymbol{r}_t,\omega)=0$ outside. By contrast, if we adopt an atomistic picture of the matter, $\chi_{\rm tip}(\boldsymbol{r}_t,\omega)$ must be expressed in terms of the *in situ* polarizabilities $\alpha_j(\omega)$ of the atoms that compose the detector

$$\chi_{\rm tip}(\boldsymbol{r}_t,\omega) = \sum_{j=1,n} \alpha_j(\omega)\delta(\boldsymbol{r}_t - \boldsymbol{r}_j). \tag{81}$$

From this last relation we can then calculate the tip–sample dispersion energy:

$$U(\boldsymbol{R}) \equiv \int_{v_{\rm tip}} \delta U(\boldsymbol{R}+\boldsymbol{r}_t)\,{\rm d}\boldsymbol{r}_t = -\tfrac{1}{2}\iint {\rm e}^{{\rm i}(\omega'+\omega'')t}\,{\rm d}\omega'\,{\rm d}\omega'' \sum_{j=1}^{n} \alpha_j(\omega)\cdot\mathcal{E}(\boldsymbol{R}+\boldsymbol{r}_j,\omega',\omega''). \tag{82}$$

Now, according to the discrete representation previously developed in section 3.2 we can further elaborate this relation. After using equations (48) and (52), and applying standard algebra procedure available in specialized textbooks (Mahanty and Ninham 1976), we can split the energy into both continuous and corrugation parts. The limit $T \longrightarrow 0$ yields

$$U(\boldsymbol{R}) = \overline{U}(\boldsymbol{R}) + \tilde{U}(\boldsymbol{R}), \tag{83}$$

where

$$\overline{U}(\boldsymbol{R}) = -\frac{2\pi C_{\rm dis}}{A}\sum_{j=1}^{n}\sum_{p}\frac{1}{4(Z+z_j+z_p)^4}, \tag{84}$$

and

$$\tilde{U}(\boldsymbol{R}) = -\frac{\pi C_{\rm dis}}{2A}\sum_{j=1}^{n}\sum_{p}\sum_{p,g_1>0,g_2\neq 0} \times\cos\boldsymbol{g}\cdot(\boldsymbol{L}+\boldsymbol{l}_j)\left(\frac{g}{2(Z+z_j+z_p)}\right)^2 K_2(g(Z+z_j+z_p)), \tag{85}$$

where the coefficients, $C_{\rm dis} = \frac{3\hbar}{\pi}\int \alpha_{\rm tip}({\rm i}u)\cdot\alpha({\rm i}u)\,{\rm d}u$, that describe the dispersion coupling efficiency between tip and surface atoms are available for a large number of atomic pairs in the literature (Vidali and Cole 1981, Ihm *et al* 1987). In spite of their simplicity, these two relations grasp the main qualitative features of the van der Waals force microscopy and thereby illustrate well how the initial FNF can give rise to lateral forces,

$$\mathcal{F}(\boldsymbol{L}, Z=cst) = -\nabla_{\boldsymbol{L}}\tilde{U}(\boldsymbol{L},Z), \tag{86}$$

modulated by the atomic rows of the sample. Near low Miller index faces of ionic crystals such corrugation forces are relatively weak (e.g. $\sim 10^{-11}$ N for a diamond tip scanning a NaCl (100) face at a constant height of 4 Å) and consequently remain difficult to detect. Recently, new

composite systems formed of $C_{60}$ thin films of ordered monolayers adsorbed on gold substrate have displayed important van der Waals corrugations ($\sim 5 \times 10^{-10}$ N) easy to detect in AFM (Sarid *et al* 1992). Simulations based on an extension of the simplified formulation we have outlined in this section were found to be in good agreement with experimental data (Girard *et al* 1993).

## 5. Controlling the near-field decay length

### *5.1. Basic concepts*

The main property of the tunnel effect (photonic or electronic) is its exponential decay versus the barrier length (see equations (63) and (73)). This important property can be directly measured with the STM or the PSTM, but also by more conventional measurements performed on metal–insulator–metal or dielectric–air–dielectric junctions of adjustable thickness. In vacuum, the *inverse decay length* $\eta$ is governed by two physical quantities: (i) the wavelength associated with the incident particles; (ii) the material parameters of the junction (optical indices or metal work function). As early as 1959, it was even suggested by Shockley that an electronic tunnel barrier could act like a filter for low incident energy of electrons (see figure 22). In other words, for a given band of energy the exponential decay of the incident wave in the barrier prevents efficient electron transfer. Following the first experimental evidence for the tunnel effect through semiconductor layered structures (Esaki and Tsu (1970), see also the Nobel Lecture by Esaki (1974)), we know that this decay can be strongly modified by adding some localized states inside the barrier. This effect is quite intriguing because the transmission coefficient $T(E)$ can reach 100% when the incident energy is resonant with the energy of one given localized state. Since the advent of the STM, many related phenomena occurring at the nanoscale have been reported. For example, metallic point contacts formed by bringing two metallic electrodes together show the expected quantum conductance of about 12.9 K$\Omega$ corresponding to the opening of one channel of conduction (Ohnishi *et al* 1998, Yanson *et al* 1998). In addition, even in the absence of actual *tunnel resonance*, many STM experiments performed above single atoms or single molecules clearly indicate enhancements of several orders of magnitude of the tunnel conductance with respect to the same measurement performed at the same tip–sample height but without adsorbate. This singular effect can be described as a *virtual resonant tunnel process* via the molecular orbitals of the adsorbate like that observed by tunnelling through a single $C_{60}$ molecule (Joachim *et al* 1995, Joachim and Gimzewski 1998). This phenomenon has also been investigated by Eigler *et al* on a simple model system: the Xe–Ni(110)system (Eigler and Schweizer 1990, Eigler *et al* 1991b, Yazdani *et al* 1996). The first unoccupied orbital 6s of Xe atom is simultaneously close to the vacuum level and far away from the metal Fermi level. In this context, these authors have succeeded in measuring the tunnel resistance of two Xe configurations:

(i) a single Xe atom located on a Ni(110) surface,

(ii) a $Xe_2$ dimer aligned perpendicularly to the same surface.

From precise tunnelling current measurements they were able to deduce a resistance of 0.1 M$\Omega$ for the monomer, and of 10 M$\Omega$ for the dimer when aligned along a direction perpendicular to the surface. These nice measurements confirm that we could intuitively predict that the resistance of a Xe wire increases with its length. In Yazdani *et al* (1996) this effect was inferred to the so-called *off-resonance conduction regime* which is nothing but the *virtual resonant process* evoked above. In spite of the absence of proper tunnel resonant effects, this virtual resonance with the 6s Xe levels produces a significant increase of the evanescent decay

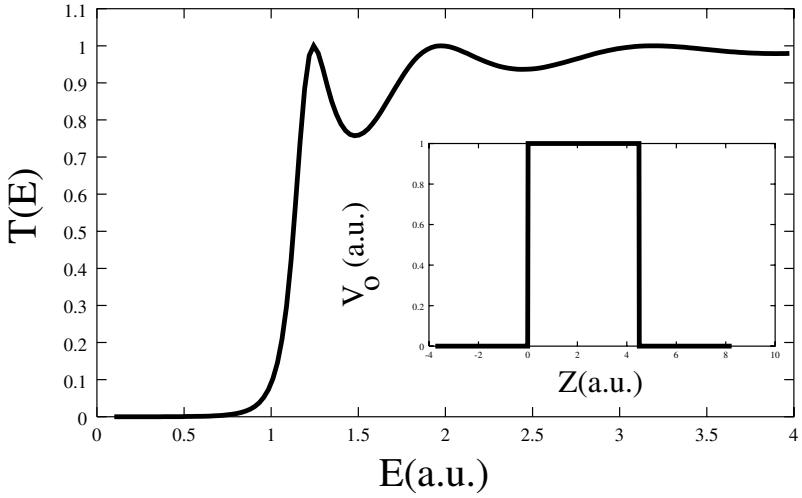


**Figure 22.** Typical transmittance of a square tunnel barrier. In this case, the barrier behaves as a high-pass filter for energy greater than the barrier height (normalized here to unity).

length through the whole junction dressed by the Xe atoms with respect to a same junction studied in the absence of atoms. Recently, new experimental evidence of nonresonant tunnel transport through molecular wires has been reported. In this case, it was even possible to spatially revolve the exponential decay law along the molecular wire by a lateral scanning of the STM tip (Langlais *et al* 1999).

In fact, these apparently singular phenomena belong to the vast class of transport phenomena through linear and partially ordered structures (Garcia and Garcia 1990, Freilikher *et al* 1996, Kemp *et al* 1994). In this context, photonic analogies have also been described in recent literature (Joannopoulos *et al* 1997, Girard *et al* 1998). After this brief introductory survey, we will revisit the physics hidden behind the control of the near-field decay length through matter.

### *5.2. Guiding the tunnel electrons*

Many experiments performed in planar geometry or with an STM junction (Giaever 1960, 1974, Mann and Kuhn 1971, Behm *et al* 1990, Güntherodt and Wiesendanger 1994) demonstrate that the tunnel effect through matter is more efficient than tunnelling through vacuum. In other words, there is always a finite energy gap in a material able to assist the tunnel transport, while in vacuum there is only a forbidden continuum of electronic states. A very simple way to describe this phenomenon is to calculate the electronic transmission coefficient through a finite series of barriers and wells. For example, with just a single localized state by quantum well (see figure 23), the system generates a new energy band just below the vacuum level. For finite value of $N$ the transmission coefficient $T(E_{\mathrm{gap}})$ between this band and the vacuum level does not fall down to zero. Moreover, the transmittance curve $T(E_{\mathrm{gap}})$ calculated around the energy gap $E_{\mathrm{gap}}$ (see figure 24) always remains significantly greater with the multi-well barrier than with the full barrier. Finally, let us note that an efficient control of the tunnel transfer efficiency through large molecules can be performed after modulation of this gap by some external action (Joachim and Gimzewski 1998). Such a control is not possible with the continuum of states existing above a free barrier.

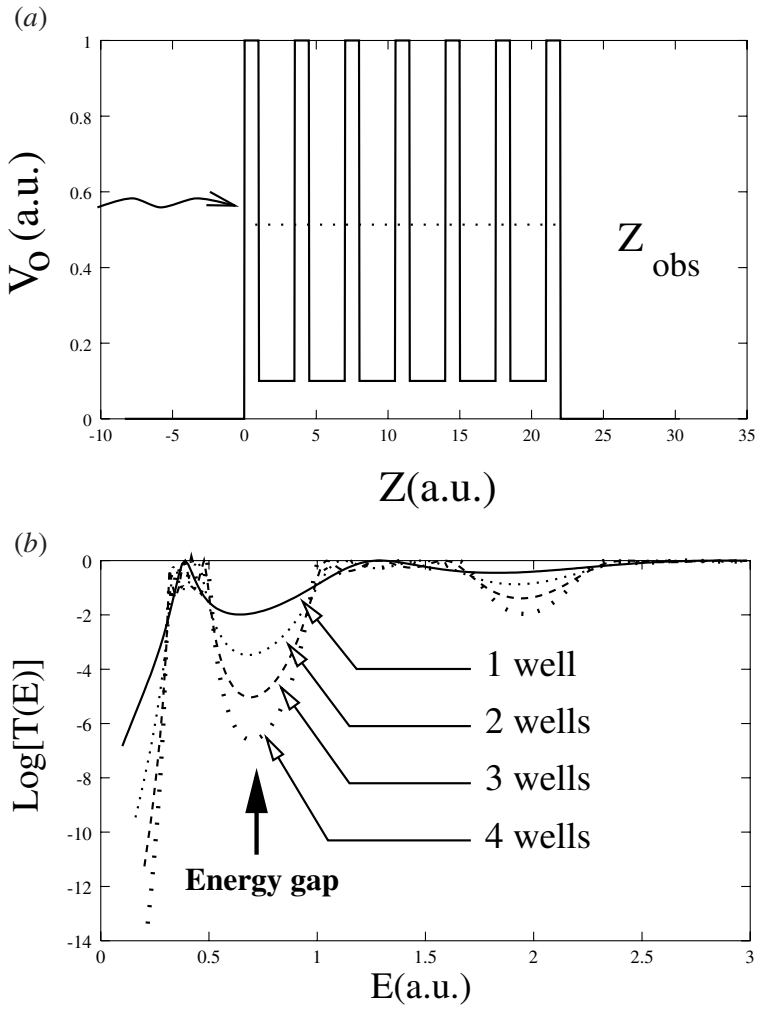


**Figure 23.** (*a*) Barrier profile used in our simulations. This profile has been chosen in order to create a single localized state in the quantum wells (dotted line). (*b*) Evolution of the transmittance with increasing number of quantum wells.

In order to get more information about the mechanisms involved in this transfer mode, we consider a linear structure made of a regular juxtaposition of elementary cells labelled respectively A and B (see figure 25). This linear juxtaposition of dimers (A–B) is a necessary condition to build up two bands separated by an energy gap. The width of this gap tends towards a finite value $\chi$ when the number $N$ of cells (A–B) goes to infinity. As in the Bragg diffraction phenomenon, the destructive interference effects are responsible for the occurrence of this forbidden band of energy. This is a general result encountered in the theory of wave propagation through ordered or partially ordered structures (Brillouin and Parodi 1956, Cohen-Tannoudji *et al* 1977). The understanding of the mechanisms that control the decay of the transmission coefficient due to these interferences has been treated in electron transfer theory (Joachim 1988) as well as for the tunnelling effect through low-gap semiconductor materials (Parker and Mead 1968). Recently, important progress in atomic and molecular wire measurements

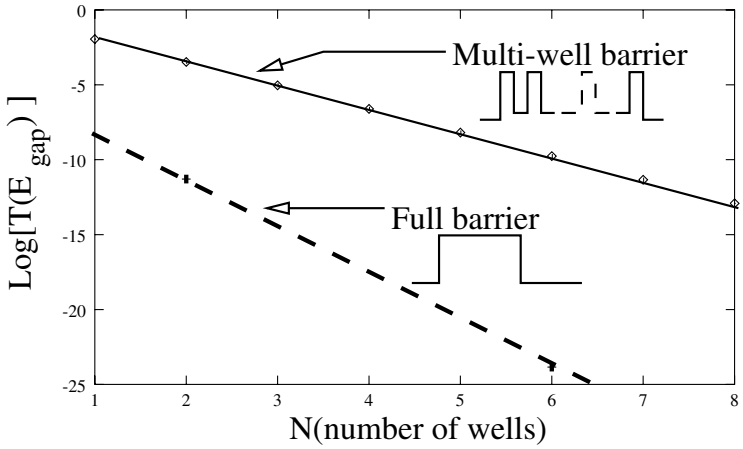


**Figure 24.** Gap transmittance of a periodically indented square tunnel barrier versus the number $N$ of indentations (cells). The geometry is given in figure 23($b$).

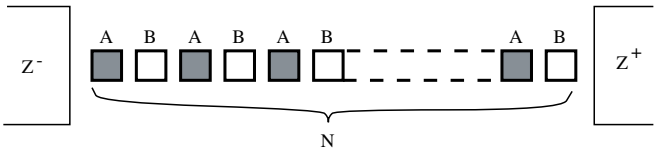


**Figure 25.** Linear periodic structure connected to two metallic pads.

(Joachim and Roth 1997) and nano-optics technology (Joannopoulos *et al* 1997, Girard *et al* 1999), has stimulated this research.

A linear sequence of (A–B) cells connected to two electrodes can provide a simple model of atomic or molecular wires (see figure 25). The transmission coefficient through the A–B chain can be written as

$$T_N(E) = |F_{11}(E)|^{-2} \tag{87}$$

where the transfer matrix $F(E)$ is a non-unitary transformation of the spatial propagator $P(z^+, z^-, E)$ defined from the left to the right part of the A–B chain (Stein and Joachim 1987). The $z^+$ and $z^-$ coordinates are defined in figure 25:

$$\begin{bmatrix} \Psi \\ \frac{\mathrm{d}\Psi}{\mathrm{d}z} \end{bmatrix}(z^+) = \mathcal{P}(z^+, z^-, E) \begin{bmatrix} \Psi \\ \frac{\mathrm{d}\Psi}{\mathrm{d}z} \end{bmatrix}(z^-) \tag{88}$$

where

$$\mathcal{P}(z^+, z^-, E) = K(z^+, E)P^+(A(E)B(E))^N P^- K(z^-, E). \tag{89}$$

The functions $\Psi(z^+)$ and $\Psi(z^-)$ represent the wavefunction amplitudes inside the two metallic pads. The elementary propagators $K(z, E)$ are defined inside the pads. The two factors $P^+$ and $P^-$ represent the interface propagators between the A–B chain and the electrodes. The expression $(A(E)B(E))^N$ labels the spatial propagator that includes the electronic couplings between all consecutive chain cells. The transfer matrix $F(E)$ can be obtained after diagonalization of the intrachain propagator $A(E)B(E)$ (Sautet and Joachim 1988). From (87), we can write

$$T_N(E) = \frac{1}{|\tilde{a}_{11}(E)\tilde{b}_{11}(E)\lambda_+(E)^N + \tilde{a}_{12}(E)\tilde{b}_{21}(E)\lambda_-(E)^N|^2} \tag{90}$$

where $\lambda_+(E)$ and $\lambda_-(E)$ are the eigenvalues associated with the matrix $A(E)B(E)$. The coefficients $\tilde{a}_{ij}(E)$ and $\tilde{b}_{ij}(E)$ represent the matrix elements of the operator $P^+$ and $P^-$ modified by the diagonalization of the propagator $A(E)B(E)$. For large but finite values of $N$, and because $\lambda_-(E) = \lambda_+(E)^{-1}$, we can write†

$$T_N(E) = T_o(E)\mathrm{e}^{-N\eta} \tag{91}$$

with

$$\eta = 2\ln(|\lambda_+(E)|) \tag{92}$$

where the exponential behaviour described in figure 24 is recovered. The secular equation giving the eigenvalue $\lambda_+(E)$ is merely the standard second-order Kramers equation $\Delta(E) = \mathrm{Tr}(A(E)B(E))^2 - 4$ (Sautet and Joachim 1988). Therefore, the tunnelling inverse decay factor in (91) is given by

$$\eta = 2\ln\left(\frac{\sqrt{\Delta(E)+4} + \sqrt{\Delta(E)}}{2}\right). \tag{93}$$

Note that for infinite wires, the $\Delta(E)$ polynomial can be used to characterize the electronic band structure of the wire: the conduction bands for $\Delta(E) < 0$ and the band gaps for $\Delta(E) > 0$. For systems of finite length, although no absolute band gap can be created, we can solve this polynomial to adjust the parameters that control the decay. We must study the $\Delta(E)$ polynomial for the energy range where $\Delta(E) > 0$. There are two interests in such a control. In a first application, one may be interested to find the chemical structure of material with a large $\Delta(E)$ able to compete with standard insulators like $SiO_2$ (Muller *et al* 1999). On the other hand, these theoretical developments can be used to devise elongated molecules with small $\Delta(E)$ in order to realize perfect molecular wires. For example, one can show that there exists a minimum accessible value of $\eta(E_g)$ depending on the energy gap between the two energy bands of the A–B chain (Magoga and Joachim 1998). Here, the parameter $E_g$ plays the role of the barrier height in tunnelling through vacuum. The second parameter that can be defined is the effective mass of the electron which controls $\eta$ and which can be used to approach the minimum available value of $\eta$ for a given $E_g$. For example, by following the method of Franz (Franz 1956) we can approximate $\Delta(E)$ by a parabolic law in the gap between the valence and the conduction band of an insulator. Since $\lambda_+(E) = \mu(E) + \mathrm{i}q(E)$ with $\mu(E) = 0$ in the gap of the molecular wire, one gets directly $q(E) = \mathrm{argsh}(\sqrt{(\Delta(E))/2})$. For $\Delta(Ef) < 4$, $q(E)$ can be expended in series of $\Delta(E)$ and $\eta(E)$ rewritten as

$$\eta(E) = 2\sqrt{\frac{2m^*(E)}{\hbar^2}\frac{(E - E_h)(E_l - E)}{\chi}} \tag{94}$$

where $m^*(E)$ represents the effective mass of the tunnelling electron in the molecular wire. $E_h$ and $E_l$ are the two energy band edges. Equation (94) generalizes the Franz two-band dispersion relationship approximation used for tunnelling in the gap of a two-band material (Franz 1956). It shows that the exponent in equation (92) for a molecular wire is controlled by three parameters: the length $L_0$ of the unit cell of the molecular wire made of a regular structure of $N$ cells, the HOMO–LUMO gap of the molecular wire and the effective mass of the tunnelling electron. Independently of the gap, this mass can be controlled by fine design of the molecular wire electronic structure (Magoga 1999).

† In this expression, the inverse decay parameter $\eta$ is dimensionless because $N$ represents the number of cells that composes the wire.

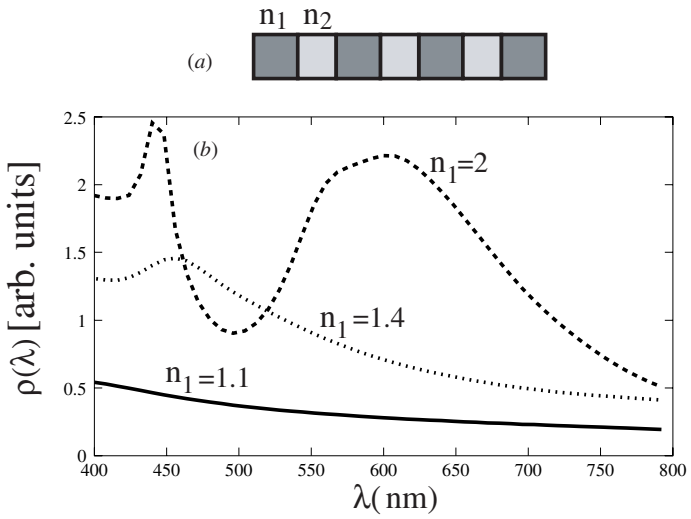


**Figure 26.** (*a*) Heterowire geometry where the cross section $\sigma = 240$ nm, $N = 4$, $l_1 = 240$ nm and $l_2 = 200$ nm resulting in a structure with a total length $L_0 = 1.560$ $\mu$m. (*b*) Variation of the integrated LDOS of different rod-shaped optical structures versus the excitation wavelength $\lambda$. The function $\rho(\lambda)$ is obtained by numerical integration of the photonic LDOS over the volume occupied by the rod described in (*a*). The three different curves have been obtained by increasing the modulation of the index of refraction $\Delta n = n_1 - n_2$. Solid curve: $\Delta n = 0$. Dotted curve: $\Delta n = 0.4$. Dashed curve $\Delta n = 1$.

### *5.3. Subwavelength photonic transport through optical constriction*

When describing the propagation of light in ordered or partially ordered mesoscopic material structures, similar phenomena can be expected. For a given band of frequencies, the decay range of evanescent waves may be commensurate with the material structure or with parts of it. In this case, high values of the transmission coefficient of electromagnetic energy can be expected. In other words, the overlap between evanescent components generated by two material structures or defects establishes the physical link that can open new optical channels. Impressive demonstrations of such collective proximity effects were extensively described in the recent literature dealing with photonic crystals (Joannopoulos *et al* 1995). As it may be intuitively understood, such periodic or pseudo-periodic materials modulate drastically the amount of transferred energy as a function of the incident frequency. For example, it was demonstrated both theoretically and experimentally that the introduction of well calibrated microcavities inside a channel waveguide, modulates the optical transmittance of an initially homogeneous waveguide (Joannopoulos *et al* 1997). The result of the modulation may be viewed as a photonic band structure in which some localized states can be created by adding localized defects in the periodic structure. Under the normal illumination condition of a propagating light beam aligned along the longitudinal axis of the channel waveguide, the introduction of new localized states can be used to create narrow transmission bands inside the photonic gaps. In the context of *near-field physics*, we know that optical tunnelling effect can be used to control the optical energy transfer between two transparent media (see previous sections 4.2.1 and 4.2.2). The so-called PSTM is based on this simple principle (Reddick *et al* 1989, Courjon *et al* 1989). As described in section 2.2, this particular illumination mode is characterized by a typical exponential decay of the detected intensity when the detector is moved away from the sample surface. The reduction of the tip to sample spacing below

the tunnelling decay length makes the energy transfer possible. Nevertheless, as has been demonstrated with a molecular wire (see section 5.2) or with a simple periodically indented barrier (see figure 24), this decay can be strongly modified by introducing some localized photon state inside the tunnel gap. In spite of similarities with tunnel electrons, some different behaviour can occur with photons. In particular, the weakness of the *equivalent potential barrier* seen by a photon travelling inside a structured dielectric medium prevents a strong localization of the particle and favours the appearence of radiative losses. In order to get more insight into this photonic analogy, let us consider the *optical heterowire* depicted in figure 26. We define the *heterowire* geometry as a rod-shaped dielectric structure which displays a variation of the optical index of refraction along its longitudinal axis. Figure 26(*a*) shows an elementary heterowire made of only two materials setting up an alternating arrangement of $N$ cells of optical index $n_1$ and $N-1$ cells of optical index $n_2$. The respective lengths of the cells along the longitudinal axis are $l_1$ and $l_2$. The cross section of the wire has a square shape of side $\sigma$. Complete spectroscopic information can be extracted from the calculation of the photonic local density of state LDOS $d(\boldsymbol{r}, \omega)$ of this sytem. This scalar quantity is deduced from the electric field susceptibility $\boldsymbol{S}(\boldsymbol{r}, \boldsymbol{r}', \omega)$ of the heterowire†

$$d(\boldsymbol{r}, \omega) = \frac{1}{\pi k_0^2} \mathrm{Im}\ \mathrm{Tr}\, \boldsymbol{S}(\boldsymbol{r}, \boldsymbol{r}, \omega) \tag{95}$$

where $k_0 = \omega/c$ is the wavevector modulus in vacuum and Im denotes the imaginary part. Solid state physics applies the concept of LDOS to nonrelativistic electrons so that the LDOS corresponds to the density of probability to find an electron of energy $\hbar\omega$ at the point $\boldsymbol{r}$ of the solid. This function is directly related to the square moduli of all possible electronic wavefunctions associated to this energy (Economou 1983). In the case of photons, different formulations of the LDOS can be proposed depending on the reference field. The most widely used formulation relies on the calculation of the electric field susceptibility. When this quantity is defined on the basis of any kind of mixed field susceptibility, such a straightforward relation to the electric field is no longer possible. However, in any case, the LDOS is the only quantitative way to describe the *continuous* part of the spectrum of any system independently of the excitation mode. In the context of optics, this means that the LDOS provides spectroscopic information which is intrinsically independent of the particular illumination mode (Martin *et al* 1999).

Using equation (95), it is now possible to determine the density of electromagnetic eigenmodes by integrating the LDOS over the volume of the optical heterowire:

$$\rho(\omega) = \int_v d(\boldsymbol{r}, \omega)\, \mathrm{d}\boldsymbol{r}. \tag{96}$$

Applying an appropriate discretization procedure on the whole volume occupied by the optical wire (Girard *et al* 1999), this last equation may be rewritten as

$$\rho(\omega) = \frac{1}{\pi k_0^2} \sum_{k=1}^{n} V_k \mathrm{Im}\ \mathrm{Tr}\, \boldsymbol{S}(\boldsymbol{r}_k, \boldsymbol{r}_k, \omega) \tag{97}$$

where $V_k$ represents the volume of the $k$th discretized cell.

For a given system, a preliminary analysis of this function allows the photonic bands to be identified (see figure 26(*b*)). Figure 26(*b*) provides a first numerical example of the evolution of the density of states of an optical heterowire versus its index modulation $\Delta n = n_1 - n_2$. The background index of refraction $n_b = \sqrt{\epsilon_b} = 1$. In this example, the second optical index $n_2$ is maintained constant with the same value as the background ($n_2 = 1$). Beyond a critical

† The general definition of this response function $\boldsymbol{S}(\boldsymbol{r}, \boldsymbol{r}, \omega)$ was given in section 2.3.

value of $\Delta n$, we observe the gradual formation of two photonic bands of eigenmodes centred on $\lambda = 450$ nm and $\lambda = 600$ nm. Note that, in the context of this report, we define a photonic band as a local increase of the DOS due to the coupling between localized photon states. Indeed, the two photonic bands of eigenmodes which show up for $n_1 = 2$ in figure 26(*b*) are not separated by a true gap which would be characterized by a vanishing LDOS. Furthermore, since we are working with structures of finite dimensions, the heterowire cannot generate an *absolute* photonic band gap independent of the incident wavevector. Nevertheless, the LDOS describes quantitatively the continuous optical spectrum of the structure. The description is not entangled with the features of any particular illumination mode. Independently of the incoming wave, the LDOS can be used for operation research purposes when optimizing the geometrical parameters $l_1$ and $l_2$ as well as the optical index modulation of a structure. From this theoretical background we can introduce the concept of a *subwavelength optical waveguide* (SOW). A SOW is obtained by inserting an optical heterowire inside a reference system (two plane dielectric slabs) (see, for example, the geometry schematized in figure 27). In order to pursue our electron–photon analogy, the reference system will be illuminated in TIR so as to couple the optical wire with an exponential decaying wave. The insertion of the heterowire will result in a SOW if it opens a transmission band in the photonic gap of the reference system. In the absence of any optical wire, the electromagnetic field state is defined by the couple of fields $\{\boldsymbol{E}_o(\boldsymbol{r}, \omega); \boldsymbol{B}_o(\boldsymbol{r}, \omega)\}$ but also by the initial field susceptibilities $\boldsymbol{S}_0$ and $\boldsymbol{Q}_0$. The application of the numerical procedure described in section 4.2.2 allows the new electromagnetic state $\{\boldsymbol{E}(\boldsymbol{r}, \omega); \boldsymbol{B}(\boldsymbol{r}, \omega)\}$, namely in the presence of the optical wires, to be defined. Figure 27 displays two maps of the electrical energy part flowing through the device for two typical wavelengths. Two important remarks must be made:

- For a wavelength chosen at the centre of the pseudo-gap (figure 27(*c*)), the energy transfer is much weaker than near resonance (see figure 27(*b*)). We are in the so-called *nonresonant tunnel regime* already mentioned in section 5.1. Note that, in spite of the absence of actual tunnel resonant effects, the evanescent decay length $\eta_{\text{junc}}^{-1}$ through the whole junction is significantly greater than the evanescent decay length in vacuum $\eta_{\text{vac}}^{-1}$. In the exemple depicted in figure 27 we have gained by about a factor of six.
- As expected, the efficiency of the tranfer increases drastically if the wavelength corresponds to the centre of the photonic band of figure 26(*a*). This increasing energy flow is accompanied by a change of direction of the incident wavevector when the optical wire is excited near resonance. In this case, we can observe the perfect commensurability existing between the variations of field intensity along the longitudinal axis of the three SOWs and the modulation of the index of refraction. In particular, the electric field pattern displays complex features, with peaks along the lateral faces of the cells of higher index of refraction. In both maps, complex fringe patterns show up. They are generated by interference between the incident surface evanescent wave and the wave scattered by the SOW.

## 6. Energy dissipation inside the near-field

### *6.1. Mean near-fields and particle transfer*

Behind the average properties of each near-field (usually detected by a local probe technique), it is important to emphasize that the associated particles are randomly exchanged, one by one, through the near-field zone between the probe tip and the surface of the material. In a permanent regime of exchange, the local probe–surface system can be viewed as a source–detector-like experiment. In this experiment, the particles are prepared in a peculiar quantum state superposition (Joachim 1987, Nakamura *et al* 1999) and transferred through the near-field

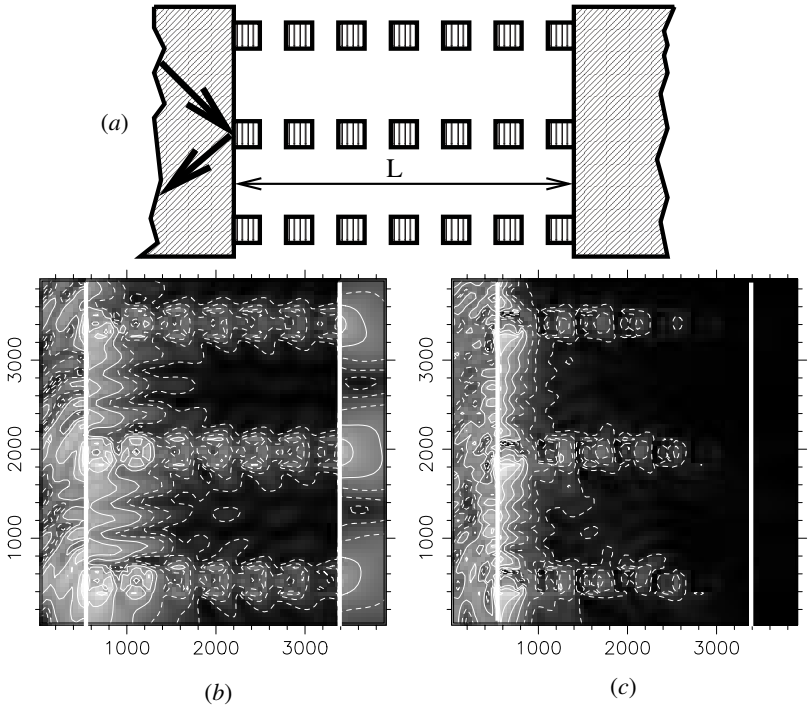


**Figure 27.** Evolution of the electric field intensity map versus the incident wavelength. Two different values have been investigated: (*b*) $\lambda = 640$ nm (resonant optical tunnel effect), (*c*) $\lambda = 475$ nm (off-resonance optical tunnel effect).

zone. For tunnelling electrons, the random character of the preparation is nicely observed by recording the power of the noise spectrum associated with the tunnelling current (Birk *et al* 1995). This Schottky noise is similar to the one recorded with a vacuum tunnel diode (Schottky 1918). It goes to zero when the transmission coefficient between the surface and the probe reaches unity (Reznikov *et al* 1995). When dealing with electron exchange, another important feature of this source–detector experiment is the Coulomb blockade effect. In a general way, even if the random exchange phenomenon between the electrodes persists, the driven electron transfer process through the near-field zone is blocked if the impedance of the source does not fit that of the junction (Holst *et al* 1994).

In NFO, the transfer process involves individual photonic particles as well. However, when working with traditional light sources (laser) this pure quantum aspect is masked by the fact that the observable electromagnetic field is an average on many photon states (Glauber 1963). Nevertheless, new single photon sources could stimulate new experiments in which photons would dwell, one by one, inside the junction during the data acquisition process (Brunel *et al* 1999).

In van der Waals force microscopy, the discrete exchange of virtual photons cannot be directly observed (Hartmann 1990, 1991, Girard and Bouju 1991). Although their role could be very important in determining the noise level in the van der Waals dispersion force measurements (Dransfeld and Xu 1988, Loomis and Maris 1994), the virtual nature of the particles exchanged precludes a direct measure in the very near-field zone.

### *6.2. Elementary inelastic processes in the near-field*

The introduction of some material in the near-field zone between the source and the detector leads to new phenomena. As already discussed in section 5, a first important phenomenon is the extension of the near-field from one electrode to the other by a proper choice of the structure introduced in the junction. Another effect results from the interaction between the transferred particles and the material located inside the near-field zone. For example, tunnelling electrons can be coupled to some vibrational modes of the material confined inside the tunnel barrier. This gives the opportunity to perform inelastic electron tunnelling spectroscopy (IETS) (Hansma 1982). In such experiments, the insulator embedded in the planar junction contains specific molecules. The transferred electrons are inelastically coupled to the vibration levels of these molecules (Hansma 1982). Different coupling mechanisms have been invoked: (i) dipole coupling for which the transferred electrons interact with the molecular oscillating dipoles at long range, (ii) direct momentum transfer on the molecule from the exchanged electrons and (iii) occupation of the molecule frontier orbitals by the transferred electrons or holes. The efficiency of these couplings increases with the dwell time in the junction.

In a local probe–surface experiment, the near-field zone is explored very locally. Consequently, the particles are constrained to be exchanged through a very small area of the junction. In IETS experiments, this means that the vibrational spectrum of a single molecule can be recorded. This must be compared with a planar IETS configuration where the most of electrons are transferred spatially far away from the molecules. In a local probe experiment, a large IETS signal was predicted (Persson and Baratoff 1987). Nevertheless, we had to wait several years for the first actual experimental evidence of this effect. Such observations were reported very recently (Stipe *et al* 1998) with $C_2H_2$ and $C_2D_2$ molecules and with CO molecules (Lauhon and Ho 1999). In these experiments, the trick consisted of including an $x$–$y$ tracking system to stabilize the STM tip over the molecule during the acquisition of the signal.

The practice of such local inelastic spectroscopies opens the way to a more active use of the transferred particles through the near-field zone. A good illustration of this phenomenon was provided by the STM study of the Xe–Ni(110) system (Eigler *et al* 1991a). It was shown that a single Xe atom could be transferred from the surface towards the tip apex by using mainly the inelastic interaction of the tunnelling electrons with the vibronic modes of the Xe trapped in its van der Waals well on the surface. It is clear here that the inelastic process does not result from some attachment of an electron to the unoccupied 6s orbital. This 6s orbital is 5 eV away from the Fermi level and the bias voltage used in this experiment is much smaller than 1 V (Eigler *et al* 1991a). An equivalent experiment was performed by Ho's group on the $C_2H_2$ molecule (Stipe *et al* 1998). In this case, inelastic tunnelling induced rotations were obtained by applying short pusle voltage to increase the tunnelling current intensity through a single $C_2H_2$ molecule adsorbed on Cu(100). Once again, the attachment of an electron on the LUMO of $C_2H_2$ turns out to be highly improbable due to the energy of the electrons involved in this experiment.

These two experiments have clearly demonstrated that the exchanged particles can be very active during the transfer process to excite rotational or vibrational modes of the material. However, such experiments cannot be interpreted as a high-resolution electron energy loss spectrocopy (HREELS) experiment (Eigler *et al* 1991a). In a HREELS experiment, the electrons are prepared in a ballistic state from a standard electron source. Therefore, the attachment process of an electron on the adsorbate can be monitored by selecting the electron incident energy. Note that similar experiments can also be performed with a local probe technique by keeping the tip apex far away from the near-field zone (e.g., in a STM

configuration, the STM tip can be transformed in a low-voltage field emission source (Watanabe *et al* 1996)). In this precise case, electrons can also be used to break a bond (Watanabe *et al* 1996) or a molecule (Dujardin *et al* 1992). However in a *pure tunnelling regime* the physics is completely different since the exchange of electrons does not follow a ballistic regime. More precisely, the intepretation of bond-breaking experiments pose the difficult problem of understanding the inelastic interactions between an incident particle devoid of *real* wavevector and the degrees of freedom (rotational, vibrational and electronic) of the molecules or any other nanostructures located in the near-field zone. Up to now, this question has not received a convincing answer and, in the context of electron tunnelling, the problem of dissipation still remains to be debated.

To close this section, let us call that this difficulty is *partially* removed in the usual context of the photon tunnelling microscopy. In this case, the fact of working with classical illumination sources drastically reduces the importance of this problem (Girard 1992). Although in the near-field zone the evanescent electromagnetic field displays important imaginary wavevector components, it may be considered as a classical quantity that will enter the coupling Hamiltonian with the status of a parameter. Consequently, in NFO a realistic prediction of the dissipation effects reduces to a proper description of the imaginary parts of either the dielectric constants of nanostructures or the molecular polarizabilities.

## 7. Conclusion and perspectives

In this review, we have tempted to unify the concept of the near-field in describing the average properties of different types of real (or virtual) particles in the presence of an interface. In a general way, the different categories of near-fields can be detected by approaching a second material very close to the sample. By reducing the lateral barrier it then becomes possible to extract local information generally out of reach by conventional methods. This is the basic principle of all *near-field microscopies and spectroscopies*.

We have explored several fundamental issues. In particular, from the understanding of the near-field concepts, we have shown how it is possible to study a new class of transport phenomena: the so-called *tunnelling transport regime*. Elongated systems for which the localization length is usually small (molecular wires, optical heterowires), can transfer particles (electrons or photons) from this mechanism.

Finally, we have shown how this localization length can be partially controlled by an appropriate structuring of the material playing the role of a near-field guide between the two interfaces. As in the other transport regimes, this opens interesting questions about the inelastic phenomena occurring in such tunnel channels. As detailed in the last section of this review, this also reopens some questions about the status of a tunnelling particle inside the near-field zone.

## Acknowledgments

We have benefited from stimulating discussions with Ch Bergaud, X Bouju, Ch Coudret, D Courjon, A Dereux, G Dujardin, A Gourdon, U Ch Fischer, J P Goudonnet, J Krenn, J P Launay, A A Lucas, M Magoga, M Orrit, O J F Martin, O Marti, Ph Sautet, M Spajer, H Tang and J C Weeber.

The authors acknowledge financial support from the CNRS Nanoscience Network initiated by the Departments SPM and SC of the CNRS. In addition, we have benefited from the computing facilities provided by the massively parallel centre CALMIP of Toulouse.

## References


Abramowitz M and Stegun I A 1970 *Handbook of Mathematical Functions* (New York: Dover)
Adamson A W 1976 *Physical Chemistry of Surfaces* (New York: Wiley)
Agarwal G S 1975 *Phys. Rev.* A **11** 230–42
——1977 *Phys. Rev.* B **15** 2371–83
Aimé J P, Michel D, Boisgard R and Nony L 1999 *Phys. Rev. Lett.* **82** 3388–91
Antoniewicz P R 1974 *Phys. Rev. Lett.* **32**
Ash E A and Nicholls G 1972 *Nature* **237** 510–2
Ashcroft N W and Mermin N D 1968 *Solid State Physics* 3rd edn (Philadelphia: Saunders College)
Balcou P and Dutriaux L 1997 *Phys. Rev. Lett.* **78** 851–4
Baratoff A 1984 *Physica* B **127** 143–50
Barchiesi D, Girard C, Martin O J F, Van Labeke D and Courjon D 1996 *Phys. Rev.* E **54** 4285–92
Behm R J, Garcia N and Rohrer H (eds) 1990 *Scanning Tunnelling Microscopy and Related Methods (NATO ASI vol E 184)* (Dordrecht: Kluwer)
Bethe H A 1944 *Phys. Rev.* **66** 163–82
Betzig E, Finn P L and Weiner S J 1992 *Appl. Phys. Lett.* **60** 2484
Binnig G, Garcia N, Rohrer H, Soler J M and Flores F 1984 *Phys. Rev.* B **30** 4816–22
Binnig G, Quate C F and Gerber C 1986 *Phys. Rev. Lett.* **56** 930–3
Binnig G and Rohrer H 1982 *Helv. Phys. Acta* **55** 726–30
Binnig G, Rohrer H, Gerber C and Weibel E 1982 *Phys. Rev. Lett.* **50** 120–4
Birk H, Jong M D and Schonenberger C 1995 *Phys. Rev. Lett.* **75** 1610–3
Born M 1921 *Z. Phys.* **7** 494
Born M and Wolf E 1964 *Principles of Optics* (Oxford: Pergamon)
Bouju X, Joachim C, Girard C and Sautet C 1993 *Phys. Rev.* B **47** 7454–61
Brillouin L and Parodi M 1956 *Propagations des Ondes dans les Milieux Périodique* (Paris: Masson–Dunod)
Brunel C, Lounis B, Tamarat P and Orrit M 1999 *Phys. Rev. Lett.* **83** 2722–5
Carniglia C K, Mandel L and Drexhage K H 1972 *J. Opt. Soc. Am.* **62** 479–86
Celli V, Marvin A and Toigo F 1975 *Phys. Rev.* B **11** 1779–86
Chavy C, Joachim C and Altibelli A 1993 *Chem. Phys. Lett.* **214** 569–75
Chen Y J, Chen W P and Burstein E 1976 *Phys. Rev. Lett.* **36** 1207
Cohen-Tannoudji C, Diu B and Laloë F 1977 *Mécanique Quantique* (Paris: Hermann)
Courjon D and Bainier C 1994 *Rep. Prog. Phys.* **57** 989–1028
Courjon D, Sarayedine K and Spajer M 1989 *Opt. Commun.* **71** 23–8
Crampin S and Bryant O R 1996 *Phys. Rev.* B **54** R17 369–70
Crommie M F, Lutz C P and Eigler D M 1993 *Science* **262** 218–20
Dereux A 1991 Théorie de l'optique de champ proche *PhD Thesis* Facultés Universitaires Notre–Dame de la Paix, Namur, Belgium
Dereux A and Pohl D 1993 The 90 degree prism edge as a model SNOM probe: near-field, photon tunnelling, and far-field properties *Near-Field Optics (NATO ASI vol E 242)* ed D Pohl and D Courjon (Dordrecht: Kluwer) pp 189–98
Dereux A, Vigneron J P, Lambin P and Lucas A A 1991 *Physica* B **175** 65–7
Dereux A, Weeber J, Bourillot E, Goudonnet J P and Girard C 1998 *Ann. Phys., Paris* C1 **23** 27–34
Descouts P and Siegenthaler H (eds) 1992 10 Years of STM *Ultramicroscopy* **42–44** 1–1670
Dransfeld K and Xu J 1988 *J. Microsc.* **152** 35–42
Dujardin G, Walkup R W and Avouris P 1992 *Science* **255** 1232–4
Duke C B 1969 *Tunnelling in Solids* (New York: Academic)
Dürig U, Pohl D W and Rohner F 1986 *J. Appl. Phys.* **59** 3318–27
Economou E 1983 *Green Functions in Quantum Physics* 2nd edn *(Springer Series in Solid-State Science vol 7)* (Berlin: Springer)
Economou E N and Ngai K L 1974 *Adv. Chem. Phys.* **27** 265–353
Eigler D M, Lutz C P and Rudge W E 1991a *Nature* **352** 600–3
Eigler D M and Schweizer E K 1990 *Nature* **344** 524–6
Eigler D M, Weiss P S, Schweizer E K and Lang N D 1991b *Phys. Rev. Lett.* **66** 1189–91
Esaki L 1957 *Phys. Rev.* **109** 603–10
——1974 *Rev. Mod. Phys.* **46** 237–44
Esaki L and Tsu R 1970 *IBM J. Res. Dev.* **14** 61–71
Esslinger T, Weidemüller M, Hemmerich A and Hänsch T W 1993 *Opt. Lett.* **18** 450–2

Fowler R and Nordheim L 1928 *Proc. R. Soc.* 173–80
Franz W 1956 *Handbook of Physics* vol 17 (Berlin: Springer) p 155
Freilikher V, Pustilnik M and Yurkevich 1996 *Phys. Rev.* B **53** 7413–6
Frenkel J 1930 *Phys. Rev.* **36** 1604–12
Furtak T E and Reyes J 1980 *Surf. Sci.* **93** 351–401
Galatry L and Gharbi T 1981 *J. Chem. Phys.* **75** 3608–16
Garcia R and Garcia N 1990 *Chem. Phys. Lett.* **173** 44–50
Gauthier S and Joachim C 1992 *Scanning Probe Microscopy: Beyond the Images* (Les Ulis, France: Les Éditions de Physique)
Giaever I 1960 *Phys. Rev. Lett.* **5** 147–50
——1974 *Rev. Mod. Phys.* **46** 245–51
Giessibl F J 1995 *Science* **267** 68–70
——1997 *Phys. Rev.* B **56** 16 010–6
Gimzewski J K, Joachim C, Schlitter R R, Langlais V, Tang H and Johannsen I 1998 *Science* **281** 531–3
Girard C 1986 *J. Chem. Phys.* **85** 6750–7
——1992 *Phys. Rev.* B **45** 1800–10
——1998 *Phys. Rev.* B **58** 12 551–4
Girard C and Bouju X 1991 *J. Chem. Phys.* **95** 2056–64
Girard C, Bouju X, Martin O J F, Dereux A, Chavy C, Tang H and Joachim C 1993 *Phys. Rev.* B **48** 15 417–24
Girard C and Courjon D 1990 *Phys. Rev.* B **42** 9340–9
Girard C and Dereux A 1996 *Rep. Prog. Phys.* **59** 657–99
Girard C, Dereux A and Joachim C 1998 *Europhys. Lett.* **44** 686–92
——1999 *Phys. Rev.* E **59** 6097–104
Girard C, Dereux A, Martin O J F and Devel M 1995 *Phys. Rev.* B **52** 2889–98
Girard C and Girardet C 1987 *J. Chem. Phys.* **86** 6531–9
Glauber R J 1963 *Phys. Rev.* **130** 2529–39
Greffet J-J and Carminati R 1997 *Prog. Surf. Sci.* **56** 133–237
Guerra J 1990 *Appl. Opt.* **29** 3741–52
Guerra J, Srinivasarao M and Stein R S 1993 *Science* **262** 1395–400
Güntherodt H-J, Anselmetti D and Meyer E (eds) 1995 *Forces in Scanning Probe Methods (NATO ASI vol E 286)* (Dordrecht: Kluwer)
Güntherodt H-J and Wiesendanger R 1993 *Theory of Scanning Tunnelling Microscopy and Related Methods* 1st edn *(Springer Series in Surface Science)* (Berlin: Springer)
——1994 *Scanning Tunnelling Microscopy: General Principles and Applications to Clean and Adsorbate–Covered Surfaces* 1st edn *(Springer Series in Surface Science)* (Berlin: Springer)
Hansma P K 1982 *Tunnelling Spectroscopy* (New York: Plenum)
Hartmann U 1990 *Phys. Rev.* B **42** 1541–6
——1991 *Phys. Rev.* B **43** 2404–7
Holst T, Esteve D, Urbina C and Devoret M H 1994 *Phys. Rev. Lett.* **73** 3455–8
Ihm G, Cole M, Toigo F and Scoles G 1987 *J. Chem. Phys.* **87** 3995–9
Israelachvilli J N and Adams E 1976 *Nature* **262** 774–7
Joachim C 1987 *Chem. Phys.* **116** 339–49
——1988 *J. Mol. Electron.* **4** 125–36
Joachim C and Gimzewski J K 1998 *Probe Microscopy* **1** 269–76
Joachim C, Gimzewski J K, Schlitter R R and Chavy C 1995 *Phys. Rev. Lett.* **74** 2102–5
Joachim C and Roth S (eds) 1997 *Atomic and Molecular Wires (NATO ASI vol E 341)* (Dordrecht: Kluwer)
Joachim C, Sautet P and Lagier P 1992 *Europhys. Lett.* **20** 697–702
Joannopoulos J D, Meade R and Winn J 1995 *Photonic Crystals* 1st edn (Princeton, NJ: Princeton University Press)
Joannopoulos J D, Villeneuve P R and Fan S 1997 *Nature* **386** 143–5
Jung L D, Campbell C T, Chinowsky T M, Mar M N and Yee S S 1998 *Langmuir* **14** 5636–48
Keller O 1996 *Phys. Rep.* **268** 85–262
Kemp M, Mujica V and Ratner M A 1994 *J. Chem. Phys.* **101** 5172–8
Klein J and Sacks W 1992 The tunnel effect prior to the STM *Scanning Probe Microscopy: Beyond the Images* (Les Ulis, France: Les Éditions de Physique)
Kliewer K L and Fuchs R 1974 *Adv. Chem. Phys.* **27** 355–541
Koglin J, Fischer U C and Fuchs H 1997 *Phys. Rev.* B **55** 7977–84
Lamoreaux S K 1997 *Phys. Rev. Lett.* **78** 5–8
Landau L D and Lifshitz E M 1960a *Field Theory* 3rd edn (London: Pergamon)

——1960b *Statistical Physics* 3rd edn (London: Pergamon)
Landauer R 1970 *Phil. Mag.* **21** 863–93
Landragin A, Courtois J-Y, Labeyrie G, Vansteenkiste N, Westbrook C I and Aspect A 1996 *Phys. Rev. Lett.* **77** 1464–7
Lang N 1969 *Solid State Commun.* **7** 1047–9
Lang N D 1986 *Phys. Rev.* B **34** 5947–57
——1994 *Surf. Sci.* **299** 284–97
Langlais V J, Schlitter R R, Gourdon H T A, Joachim C and Gimzewski J K 1999 *Phys. Rev. Lett.* **83** 2809–12
Lauhon L J and Ho W 1999 *Phys. Rev.* B **60** R8525–8
Li J, Schneider W D, Berndt R and Crampin S 1998 *Phys. Rev. Lett.* **80** 3332–5
Lifshitz E M 1956 *Sov. Phys.–JETP* **2** 73–83
London F 1930 *Z. Phys.* **63** 245–55
Loomis J J and Maris H J 1994 *Phys. Rev.* B **50** 18 517–24
Lucas A A 1990 *Europhys. News* **21** 63–7
Lucas A A, Morawitz H, Henry G R, Vigneron J-P, Lambin P, Cutler P H and Feuchtwang T E 1988 *Phys. Rev.* B **37** 10 708–20
Lucas A A, Vigneron J P, Dereux A and Derycke I 1994 *Le Vide, les Couches Minces* **272** 193–5
Lucas A A, Vigneron J P, Lambin P, Laloyaux T and Derycke I 1992 *Surf. Sci.* **269**
Lukosz W and Kunz R E 1977 *J. Opt. Soc. Am.* **67** 1607–14
Maclachlan A D, Gregory R D and Ball M A 1963 *Mol. Phys.* **7** 119–24
Madelung E 1919 *Z. Phys.* **2** 494
Magoga M 1999 Étude du transport tunnel à travers une seule molécule *PhD Thesis* Université Paul Sabatier, Toulouse III, France
Magoga M and Joachim C 1998 *Phys. Rev.* B **57** 1820–3
Mahanty J and Ninham B W 1973 *J. Chem. Phys.* **59** 6157
——1976 *Dispersion Forces* (London: Academic)
Mann B and Kuhn H 1971 *J. Appl. Phys.* **42** 4398
Maradudin A A and Zierau W 1976 *Phys. Rev.* B **14** 484–99
Marti O and Möller R (eds) 1995 *Photons and Local Probes (NATO ASI vol E 300)* (Dordrecht: Kluwer)
Martin O J F, Girard C and Dereux A 1995 *Phys. Rev. Lett.* **74** 526–9
Martin O J F, Girard C, Smith D R and Schultz S 1999 *Phys. Rev. Lett.* **82** 315–8
Mavroyannis C 1963 *Mol. Phys.* **6** 593–603
Metiu H 1984 *Prog. Surf. Sci.* **17** 153–320
Muller D A, Sorsch T, Moccio S, Baumann F H, Evans-Lutthrodt K and Timp G 1999 *Nature* **399** 758–61
Nakamura Y, Pashkin Y A and Tsai J S 1999 *Nature* **398** 786–9
Ohnishi H, Kondo Y and Takayanagi K 1998 *Science* **395** 780–2
Otto A 1968 *Z. Phys.* **216** 398–410
Parker G H and Mead C A 1968 *Phys. Rev. Lett.* **21** 605–8
Pendry J B, Prêtre A, Rous P J and Martin-Moreno L 1991 *Surf. Sci.* **244** 160
Persson B N J and Baratoff A 1987 *Phys. Rev. Lett.* **59** 339–42
Pettinger B, Tadjeddine A and Kolb D M 1979 *Chem. Phys. Lett.* **66** 544–50
Pizzagalli L, Joachim C, Bouju X and Girard C 1997 *Europhys. Lett.* **38** 97–102
——1998 *Appl. Phys.* A **66** S875–8
Pohl D and Courjon D (eds) 1993 *Near-Field Optics (NATO ASI vol E 242)* (Dordrecht: Kluwer)
Pohl D W, Denk W and Lanz M 1984 *Appl. Phys. Lett.* **44** 651–3
Reddick R C, Warmack R J and Ferrell T L 1989 *Phys. Rev.* B **39** 767–70
Reznikov M, Heilblum M, Shtrikman H and Mahalu D 1995 *Phys. Rev. Lett.* **75** 3340–3
Rugar D and Hansma P 1990 *Phys. Today*
Ruppin R 1973 *Surf. Sci.* **34** 20–31
Sabisky E S and Anderson C H 1973 *Phys. Rev.* A **7** 790
Sacks W, Gauthier S, Rousset S, Klein J and Esrick M A 1987 *Phys. Rev.* B **36** 961
Sarid D, Chen T, Howells S, Gallagher M, Yi L, Lichtenberger D L, Nebesney K W, Ray C D, Huffman D R and Lamb L D 1992 *Ultramicroscopy* **42**
Sautet P and Bocquet M L 1994 *Surf. Sci. Lett.* **304** L445–50
——1996 *Phys. Rev.* B **53** 4910–25
Sautet P and Joachim C 1988 *Phys. Rev.* B **38** 12 238–48
——1991 *Chem. Phys.* **185** 23–30
——1992 *Surf. Sci.* **271** 387–94

Schottky W 1918 *Ann. Phys., Lpz.* **57** 541–51
Shluger A L, Rohl A, Wilson R M and Williams R T 1995 *J. Vac. Sci. Technol.* B **13** 1155–62
Shluger A L, Wilson R M and Williams R T 1994 *Phys. Rev.* B **49** 4915–30
Shockley W 1959 Electrons and Holes in Semiconductors (With Application to Transistor Electronics) (Princeton, NJ: Van Nostrand-Reinhold)
Solymar L 1972 *Superconductive Tunnelling and Applications* (London: Chapman and Hall)
Sommerfeld A 1909 *Ann. Phys., Lpz.* IV **28** 665–737
Steele W A 1974 *The Interaction of Gases with Solid Surfaces* (Oxford: Pergamon)
Stein J and Joachim C 1987 *J. Phys. A: Math. Gen.* **20** 2849–54
Stipe B C, Rezaci M A and Ho W 1998 *Science* **279** 1907–9
Stoll E 1984 *Surf. Sci. Lett.* **143**
Stoll E, Baratoff A, Selloni A and Carnevali P 1984 *J. Phys. C: Solid State Phys.* **17** 3073
Tabor D and Winterton R H S 1969 *Proc. R. Soc.* **312** 435–45
Tang H, Bouju X, Joachim C, Girard C and Devillers J 1998 *J. Chem. Phys.* **108** 359–67
Tekman E and Ciraci S 1989 *Phys. Rev.* B **40** 10 286–93
Tersoff J and Hamann D R 1985 *Phys. Rev.* B **31** 805–13
Toigo F, Marvin A, Celli V and Hill N R 1977 *Phys. Rev.* B 5618–26
Tsukada M, Kobayashi K and Isshiki N 1991a *Surf. Sci.* **242** 12–22
Tsukada M, Kobayashi K, Isshiki N and Kageshima H 1991b *Surf. Sci. Rep.* **13** 265–304
van Hulst N F, Moers M H and Bölger B 1993 *J. Microsc.* **171** 95–105
Van Labeke D and Barchiesi D 1992 *J. Opt. Soc. Am.* **9** 732–9
——1993 Theoretical problems in scanning near-field optical microscopy *Near-Field Optics (NATO ASI vol E 242)* ed D Pohl and D Courjon (Dordrecht: Kluwer) pp 157–78
Vidali G and Cole M W 1981 *Surf. Sci.* **110** 10–8
Vigoureux J M, Girard C and Courjon D 1989 *Opt. Lett.* **14** 1039–42
Ward A J and Pendry J B 1997 *J. Mod. Opt.* **44** 1703–14
Watanabe S, Ono Y A, Hashizume T and Wada Y 1996 *Phys. Rev.* B **54** R17 308–11
Weeber J, Bourillot E, Dereux A, Chen Y, Goudonnet J-P and Girard C 1996 *Phys. Rev. Lett.* **77** 5332–5
Weeber J C 1996 Diffraction en champ proche optique. Analyse des images de microscopies à effet tunnel phononique *PhD Thesis* Burgundy University, Dijon, France
Yanson A I, Rubio Bollinger G, van dem Brom H E, Agrait N and Ruitenbeek J M 1998 *Science* **395** 783–5
Yazdani A, Eigler D M and Lang N D 1996 *Science* **272** 1921–4
Zangwill A 1988 *Physics at Surfaces* (New York: Cambridge University Press)
Zenneck J 1907 *Ann. Phys., Lpz.* IV **23** 846
Ziman J M 1964 *The Physics of the Metals* (Cambridge: Cambridge University Press)